ClimateAR: Multi-Scale Autoregressive Generative Modeling for Seasonal-to-Interannual Climate Forecasting

Anonymous authors
Paper under double-blind review

Abstract

Accurate Seasonal-to-interannual climate forecasting provides critical support for decision-making in agriculture, energy, and disaster preparedness. Current deterministic models often fail to capture climate uncertainty, while existing generative approaches oversimplify the system by neglecting key spatiotemporal dependencies and cross-scale interactions. To address these limitations, we introduce **ClimateAR**, an AutoRegressive generative model for probabilistic Climate forecasting. The framework incorporates two novel components: (1) an aligned tokenizer that bridges and aligns heterogeneous simulation and real-world data to improve transferability across domains, and (2) a mixed-scale conditioning mechanism that captures multi-scale climate interactions for robust probabilistic forecasting. Extensive evaluations on the ERA5 reanalysis dataset show that ClimateAR achieves state-of-the-art performance, improving anomaly correlation skill by 29.27% on average compared to leading baselines. Code is available at `https://anonymous.4open.science/r/ClimateAR-956D`.

1 Introduction

Seasonal-to-interannual (S2I) Climate forecasting aims to predict the evolution of the climate system from several months to roughly several years timescales. It provides critical guidance for a wide range of applications, including resource allocation, energy management, and agricultural planning (Meehl et al., 2021). In contrast to weather forecasting, climate prediction focuses on statistical features of anomaly fields over extended periods, which are intrinsically uncertain due to the complex, nonlinear, and chaotic dynamics of the Earth system. As the forecast horizon extends beyond the weather scale (e.g., >1 month), the sources of predictability of the climate system undergo a fundamental transition: short-term, grid-resolved meteorological signals diminish in influence, giving way to slower-evolving modes of internal climate variability (Trenberth et al., 2007). A prime example is the El Niño–Southern Oscillation (ENSO), whose evolution is governed by nonlinear ocean-atmosphere interactions and modulated by stochastic atmospheric transients (Amaya et al., 2025), leading to significant irreducible uncertainty. Thus, probabilistic forecasting offers more realistic descriptions of inherent uncertainty in climate systems and thus improves the predictive skill for the possibilities of occurrence of extreme events (Price et al., 2025).

Over the past decades, Numerical Weather Prediction (NWP) models have significantly advanced climate and weather forecasting by numerically solving the governing equations of atmospheric and oceanic dynamics (Hurrell et al., 2013; Zhang et al., 2019). These physics-based systems offer strong interpretability and long-term stability, rooted in first principles. However, they face inherent trade-offs between computational cost and spatial resolution, which constrain their ability to scale to high-resolution global simulations—particularly for ensemble or real-time applications (Guo et al., 2025). Recently, data-driven approaches based on deep learning have emerged as a promising alternative (Hwang et al., 2019; Lam et al., 2023; Nguyen et al., 2023; Bi et al., 2023; Liu et al., 2025). By learning complex spatiotemporal patterns directly from reanalysis datasets, they achieve greater computational efficiency and good accuracy in short- to medium-range forecasting. Nevertheless, most existing deep learning methods operate at the pixel (or grid) level and produce deterministic outputs, thereby failing to capture the probabilistic nature of climate variability and underrepresenting uncertainty in long-range predictions.

To address this gap, probabilistic methods based on generative adversarial networks (GANs) (Ravuri et al., 2021; Zhang et al., 2023) and diffusion models (Price et al., 2025; Brenowitz et al., 2025) have been introduced. These methods explicitly represent uncertainty by modeling the joint distribution of climate variables, enabling ensemble predictions. Yet, they frequently treat the climate system as an oversimplified monolithic stochastic process, potentially overlooking essential multi-scale spatiotemporal correlations. For example, they may fail to capture the energy cascade from large-scale climate modes (e.g., ENSO) to regional weather anomalies, a key mechanism governing seasonal predictability (Amaya et al., 2025).

In this paper, we explore the visual autoregressive (AR) model (Tian et al., 2024; Xiong et al., 2024; Li et al., 2024; Han et al., 2025) for the probabilistic modeling of S2I climate forecasting. By representing images as sequences of discrete tokens across multiple scales, AR models capture rich semantic and spatial dependencies while avoiding oversimplified stochastic assumptions. Crucially, the multiscale inductive bias is particularly useful to model climate systems, where phenomena such as teleconnections (i.e., large-scale and statistically significant relationships between climate anomalies in geographically distant regions) and scale interactions are fundamental. In addition, the token classification-based generative process is naturally aligned with climate forecasting, where accuracy and physical consistency are prioritized over diversity.

Despite its theoretical promise, adapting the visual AR model to climate forecasting faces two major challenges: (1) **Highly heterogeneous meteorological data.** Due to data limitations, a common training paradigm in climate research (Nguyen et al., 2023) involves pre-training on simulated data (e.g., CMIP6 (Eyring et al., 2016a)) and fine-tuning on reanalysis data (e.g., ERA5 (Hersbach et al., 2023)). However, the distribution discrepancy between the simulated and reanalysis data hinders effective model transfer. Standard visual tokenizers in AR models treat inputs as homogeneous channels (Esser et al., 2021), lacking mechanisms to align semantic representations across domains. (2) **Complex conditional modeling.** Climate forecasts depend on accurately conditioning the generative process on the prior climatic state—a high-dimensional, multi-variable field with extremely high information density. Effectively integrating such complex conditions is challenging, particularly when capturing cross-scale interactions that govern large-scale predictability in climate dynamics, such as the teleconnections. In contrast, typical existing generative conditioning mechanisms, designed for low-dimensional inputs like text prompts, lack the capacity to handle teleconnection and fail to effectively inject complex climatic constraints (Pang et al., 2024).

To overcome these challenges, we propose **ClimateAR**, the first AutoRegressive model designed for probabilistic Climate forecasting. ClimateAR incorporates a novel tokenization strategy and a mixed-scale conditioning mechanism to handle heterogeneous, high-dimensional climate data. The main contributions of ClimateAR are as follows:

- A principled **generative approach** to probabilistic climate forecasting. ClimateAR models the climate system as a multi-scale stochastic process, enabling the generation of ensemble forecasts that capture inherent climate uncertainty and provide a realistic description of climate processes.

- An **aligned tokenizer** that adopts vector quantization with segmented codebooks to represent high-dimensional climate variables efficiently. A shallow-separation and deep-sharing architecture aligns token semantics across simulated and real-world datasets, enhancing transferability.

- A **mixed-scale conditional control** mechanism that combines scale-specific local guidance with a hybrid-scale global prompt, capturing cross-scale interactions (e.g., the influence of large-scale oceanic anomalies on regional temperature) and leveraging high-information-density conditions effectively.

- Extensive experiments on ERA5 reanalysis data demonstrate that ClimateAR outperforms state-of-the-art AI and physical baselines, achieving an average 29.27% improvement in correlation skill. Notably, it exhibits strong performance in forecasting El Niño–Southern Oscillation (ENSO) indices, highlighting its ability to capture essential climate modes.

2 RELATE WORK

Deep learning methods have demonstrated significant advantages over traditional numerical approaches for weather and climate forecasting (Ren et al., 2021; Chen et al., 2023b; Shi et al., 2025). Recent advances leverage sophisticated models to capture more representative meteorological signals, leading to improved accuracy. For example, Pangu (Bi et al., 2023), ClimaX (Nguyen et al., 2023), and Aurora (Bodnar et al., 2025) employ vision Transformers, while GraphCast (Lam et al., 2023) and Oneforecast (Gao et al., 2025) utilize GNNs. In addition, Fuxi (Chen et al., 2023a) and FuXi-S2S (Chen et al., 2024) leverage FNOs. Beyond purely data-driven models, some deep learning approaches also attempt to incorporate physical knowledge to better capture the underlying dynamics of the climate system. For example, ClimODE (Verma et al., 2024) integrates conservation equations, SFNO (Bonev et al., 2023) adopts the spherical characteristics of Earth, and WeatherGFT (Xu et al., 2024) uses PDE kernels. However, these models typically focus on capturing pixel-level patterns and produce deterministic forecasts, often neglecting the inherent uncertainty of the climate system. To address this gap, several approaches have explored generative models for stochasticity modeling. Notable examples include GANs-based methods (cDCGAN (Sha et al., 2024) and cGAN (Rampal et al., 2024)), and models based on diffusion processes (Graph-EFM (Oskarsson et al., 2024), GenCast (Price et al., 2025), and GenAI (Lopez-Gomez et al., 2025)). However, these methods often treat the climate system as an overly simplified stochastic process, potentially overlooking critical multi-scale spatiotemporal correlations.

3 PRELIMINARY

Problem Definition. Following standard climate forecasting settings (Meehl et al., 2021; Arias et al., 2021), we adopt monthly-averaged meteorological data as both input and output of the model. The input is an initial climate state $\mathbf{X}_t \in \mathbb{R}^{C\times H\times W}$ at time step t, where C represents the number of meteorological variables, H and W represent the height and width of the global latitude-longitude grid, respectively. For the generative model, the forecasting task is to model the probabilistic distribution of all variables at the subsequent time step:

$$p(\mathbf{X}_{t+1} \mid \mathbf{X}_t) = \mathcal{F}(\mathbf{X}_t, \Theta), \tag{1}$$

where $\mathcal{F}$ represents the neural network, Θ is the learnable parameters of $\mathcal{F}$. Then, long-term forecasts $\mathbf{X}_{t+T}$ can be obtained through a T-step iterative forecasting process.

Simulation to Real-World Transfer. Existing works have demonstrated that pre-training models with simulated data can significantly enhance performance (Nguyen et al., 2023). Due to the limited availability of long-term observational and reanalysis data, it is challenging to train deep climate models from scratch with sufficient generalization ability. To overcome this data scarcity, we leverage large-scale simulated data from the Coupled Model Intercomparison Project Phase 6 (CMIP6) (Eyring et al., 2016a) during pre-training. This allows the model to learn robust physical patterns and climate dynamics, providing a strong foundational prior. Subsequently, we transfer the model to real-world forecasting by fine-tuning on the ERA5 dataset (Hersbach et al., 2023), augmented with ocean variables from Ocean Reanalysis System 5 (ORAS5) (Zuo et al., 2019) to enhance physical consistency. This simulated-to-real transfer strategy effectively bridges the distribution gap while capitalizing on the complementary strengths of simulated and observed climate data. Thus, our model can integrate diverse variables and possess robust cross-domain alignment capabilities between different data sources.

Visual Autoregressive Modeling. Tian et al. (2024) proposed a novelty paradigm named VAR for visual autoregressive modeling. The tokenizer first encodes the input image $\mathbf{I} \in \mathbb{R}^{H\times W\times C}$ into a continuous feature map $\mathbf{f} \in \mathbb{R}^{h\times w\times d}$, and then quantizes it into K multi-scale residual discrete token maps $(\mathbf{r}_1, \mathbf{r}_2, \ldots, \mathbf{r}_K)$ with their corresponding resolution $(h_1, w_1) < (h_2, w_2) < \cdots < (h_K, w_K) = (h, w)$:

$$\mathbf{f} = \varepsilon(\mathbf{I}), \quad \mathbf{res}_k = \mathbf{f} - \sum_{i=1}^{k-1} \mathrm{up}(\mathbf{r}_i, (h, w)), \quad \mathbf{r}_k = \underset{q\in\{1,\ldots,V\}}{\arg\min} \left\|\mathbf{res}_k - \mathbf{c}_q\right\|_2, \tag{2}$$

where ε is an encoder, $\mathbf{res}_k$ is the residual feature map before quantization, $\mathbf{c}_q$ represents the q-th vector in the codebook with V capacity, and $\mathrm{up}(\cdot)$ denotes an upsampling operation. Then, the

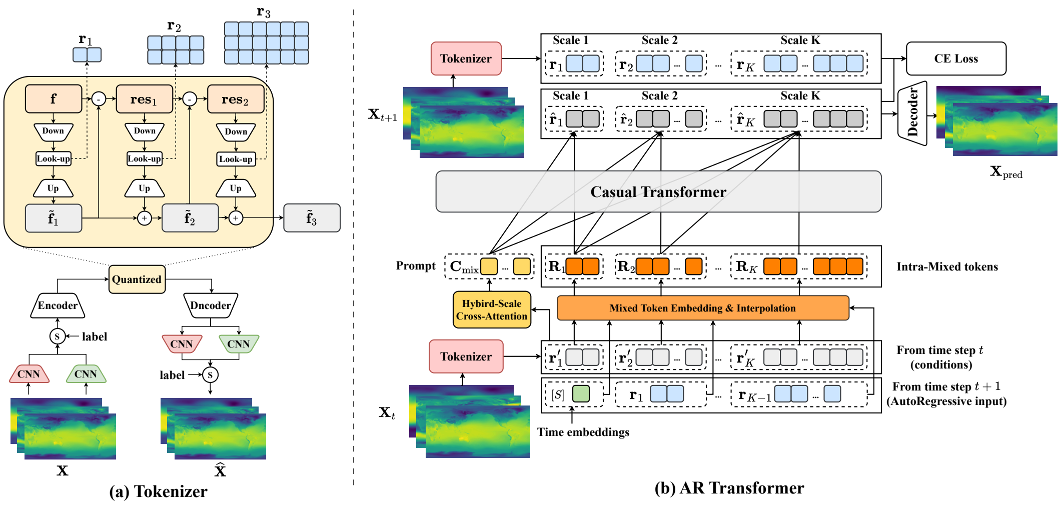

(a) Tokenizer

(b) AR Transformer

Figure 1: The architecture of ClimateAR consists of two key components: (a) a VQ multi-scale tokenizer where **S** replaces a selection operation by label of data source. (b) a decoder-only autoregressive transformer where **CE** represent the cross-entropy loss function.

feature map $\tilde{\mathbf{f}}_k$ at k-th scale and the reconstructed image can be expressed as:

$$\tilde{\mathbf{f}}_k = \sum_{i=1}^{k} \text{up}(\mathbf{r}_i, (h, w)), \quad \hat{\mathbf{I}} = \mathcal{D}(\tilde{\mathbf{f}}), \tag{3}$$

where $\tilde{\mathbf{f}} = \tilde{\mathbf{f}}_K$ is the feature map after quantized, $\mathcal{D}$ is a decoder, and $\hat{\mathbf{I}}$ is the reconstructed image. Subsequently, VAR redefines the paradigm of visual autoregressive modeling via the next-scale token map prediction:

$$p(\mathbf{r}_1, \mathbf{r}_2, ..., \mathbf{r}_K) = \prod_{k=1}^{K} p(\mathbf{r}_k \mid \mathbf{r}_{<k}), \tag{4}$$

where $\mathbf{r}_{<k}$ represents token maps prior to scale k.

4 Methodology

As illustrated in Fig. 1, ClimateAR consists of a tokenizer and an autoregressive transformer. Given an initial climate state $\mathbf{X}_t$, the tokenizer first encodes it into a sequence of multi-scale token maps $(\mathbf{r}'_1, \mathbf{r}'_2, ..., \mathbf{r}'_K)$, which serve as conditional inputs. The autoregressive transformer then generates the forecast iteratively: starting from a learnable start token $[\mathbf{S}]$, it produces subsequent token maps scale by scale, with each step conditioned on previously generated tokens and the corresponding scale-specific features. To further guide the generation process globally, the conditional token maps are compressed into a hybrid-scale prompt that acts as a prefix across all scales. Finally, the decoder reconstructs the future climate state $\mathbf{X}_{t+1}$ from the full set of predicted token maps.

4.1 Tokenize Heterogeneous Meteorological Data

High-Dimensional Feature Extraction. Following vector-quantized (VQ) methods, we encode multivariate climate data $\mathbf{X}_t \in \mathbb{R}^{C \times H \times W}$ into a sequence of multi-scale discrete token maps $(\mathbf{r}_1, \mathbf{r}_2, ..., \mathbf{r}_K)$. Given the high dimensionality and intense information of typical meteorological variables, we adopt a partitioned quantization strategy to enhance codebook capacity and reduce latent feature dimension. Specifically, the residual feature $\mathbf{res}_k \in \mathbb{R}^{h \times w \times d}$ at scale k is split along the channel dimension into N disjoint segments, and each of them is quantized independently using a separate codebook of size V:

$$\mathbf{res}_k = [\mathbf{res}_k^{(1)}, \mathbf{res}_k^{(2)}, \ldots, \mathbf{res}_k^{(N)}], \quad \mathbf{res}_k^{(n)} \in \mathbb{R}^{h \times w \times d_n} \tag{5}$$

$$\mathbf{r}_k^{(n)} = \underset{q \in \{1, \ldots, V\}}{\arg\min} \left\| \mathbf{res}_k^{(n)} - \mathbf{c}_q^{(n)} \right\|_2, \tag{6}$$

where $\sum_{n=1}^{N} d_n = d$. This partition increases the effective codebook capacity from V to V^N while reducing the per-segment feature dimension to d/N, making the model both expressive and computationally tractable. Each token $\mathbf{r}_k^{(i,j)}$ is thus represented by N disjoint labels during autoregressive training.

Cross-Domain Alignment. To enable knowledge transfer from simulation-based pre-training to real-world forecasting, we design an **aligned VQ tokenizer** that projects heterogeneous climatic data—from simulated and real-world sources—into a shared semantic space. As illustrated in Fig. 1, we employ domain-specific convolutional layers in the initial stages of the encoder and the final stages of the decoder to handle low-level distribution discrepancy, while sharing deep network layers and codebooks across domains to ensure high-level climate patterns are encoded consistently. This "shallow-separation, deep-alignment" design promotes learning transferable and domain-invariant representations, improving generalization when fine-tuning on real observations.

4.2 Conditional Control

To effectively incorporate multi-scale climatic dependencies into the generative process, we condition the autoregressive generation with multi-scale information from the previous state. Specifically, the tokenizer encodes both the initial state $\mathbf{X}_t$ and the target state $\mathbf{X}_{t+1}$ into multi-scale token sequences $(\mathbf{r}'_1, \mathbf{r}'_2, ..., \mathbf{r}'_K)$ and $(\mathbf{r}_1, \mathbf{r}_2, ..., \mathbf{r}_K)$, respectively. The conditional distribution $p(\mathbf{X}_{t+1} \mid \mathbf{X}_t)$ can be expressed autoregressively over scales:

$$p(\mathbf{X}_{t+1} \mid \mathbf{X}_t) = p(\mathbf{r}_1, \mathbf{r}_2, ..., \mathbf{r}_K \mid \mathbf{r}'_1, \mathbf{r}'_2, ..., \mathbf{r}'_K) = \prod_{k=1}^{K} p(\mathbf{r}_k \mid \mathbf{r}_{<k}, \mathbf{r}'_{\leq K}). \tag{7}$$

Intra-scale Mixed Token. Directly conditioning on all scales poses convergence challenges due to the high information density of climate states. We therefore introduce a *intra-scale mixed-token* mechanism that fuses the autoregressive feature $\tilde{\mathbf{f}}_{k-1}$ (reconstructed from tokens $\mathbf{r}_{\leq k-1}$ through Eq. 3) and with the conditional feature $\tilde{\mathbf{f}}'_k$ from $\mathbf{r}_{\leq k}$ at each scale. This allows the model to approximate the conditional distribution as:

$$\mathbf{R}_k = \text{Concat}\Big(\text{down}(\tilde{\mathbf{f}}_{k-1}, (w_k, h_k)), \text{down}(\tilde{\mathbf{f}}'_k, (w_k, h_k))\Big), \tag{8}$$

$$p(\mathbf{r}_k \mid \mathbf{r}_{<k}, \mathbf{r}'_{\leq K}) \approx p(\mathbf{r}_k \mid \mathbf{R}_{\leq k}), \tag{9}$$

where $\text{down}(\cdot)$ performs spatial interpolation to match the target token resolution and $\mathbf{R}_k$ represents the mixed token at scale k. This approximation effectively maintains scale-wise physical consistency while leveraging the efficiency of a standard autoregressive framework.

Hybrid-Scale Prompt. While the intra-scale mixed token aligns conditional information at corresponding scales, the autoregressive process inherently lacks access to subsequent finer-scales $(\mathbf{r}'_{>k})$ conditional information. This presents a significant limitation for climate forecasting, as the evolution of large-scale climate phenomena (e.g., ENSO) is often modulated by finer-scale processes (e.g., regional convective activity or oceanic eddies). To capture these interactions, we propose a hybrid-scale prompt $\mathbf{C}_{\text{mix}}$ that compresses global, multi-scale information from the entire conditional token sequence into a global context using cross-attention:

$$\mathbf{C}_{\text{mix}} = \text{Attention}(q = \mathbf{q}, kv = (\mathbf{r}'_1, \mathbf{r}'_2, ..., \mathbf{r}'_K)), \tag{10}$$

where $\mathbf{q}$ is a learnable hybrid-scale query sequence. The resulting representation serves as a prefix to the autoregressive sequence, enabling full cross-scale awareness. It is important to note that the compressed $\mathbf{C}_{mix}$ resides in a continuous space, whereas $(\mathbf{r}'_1, \mathbf{r}'_2, ..., \mathbf{r}'_K)$ are discrete tokens. Therefore, even though $\mathbf{C}_{mix}$ is much shorter, we can still achieve nearly lossless compression of hybrid-scale information. The exact conditional generation thus becomes:

$$p(\mathbf{r}_k \mid \mathbf{r}_{<k}, \mathbf{r}'_{\leq K}) = p(\mathbf{r}_k \mid \mathbf{C}_{\text{mix}}, \mathbf{R}_{\leq k}). \tag{11}$$

Finally, we apply a decoder-only transformer to the entire token maps $[\mathbf{C}_{mix}, \mathbf{R}_1, \mathbf{R}_2, ..., \mathbf{R}_k]$ to obtain next-scale token prediction $\mathbf{r}_k$.

Noise-Augmented Teacher-Forcing. Autoregressive models trained with teacher forcing are prone to *exposure bias*: during training, the model uses ground-truth tokens as input, while during inference it must use its own predictions, leading to error accumulation. To mitigate this issue, during training, we stochastically replace ground-truth tokens with random tokens during training while preserving the residual structure across scales:

$$\mathbf{res}_k = \mathbf{f} - \sum_{i=1}^{k-1} \mathrm{up}(\mathbf{r}_i^{\mathrm{noisy}}, (h, w)),\ \mathbf{r}_k = \underset{q \in \{1, \dots, V\}}{\arg\min} \left\| \mathbf{res}_k - \mathbf{c}_q \right\|_2, \tag{12}$$

$$\mathbf{r}_k^{\mathrm{noisy}} = \mathbf{r}_k \odot \mathbf{M} + \mathbf{r}_q \odot (1 - \mathbf{M}), \tag{13}$$

where $\mathbf{M}_{i,j} \sim B(1, p)$ is a mask for whether the element of $\mathbf{r}_k^{i,j}$ should be replaced by a random token $\mathbf{r}_q^{i,j}$, $\odot$ represents Hadamard product, and more details are in Appendix A.1. Introducing such noise in autoregressive conditions narrows the gap between training and inference, and forces the model to rely more heavily on the conditional state $\mathbf{X}_t$ to reconstruct the target state, thus enhancing its ability to correct the accumulated errors.

4.3 Training Procedure

VQ-VAE Training: We first train the VQ-VAE on a mixture of real-world (ERA5, ORAS5) and simulated (CMIP6) climate data. Domain indicators are included to facilitate the cross-domain alignment described in Section 4.1. Once trained, the VQ-VAE weights are frozen, and the model serves as a fixed tokenizer for encoding input states and decoding predicted tokens. The training objective combines VQ loss with perceptual terms:

$$\mathcal{L} = \left\| \mathbf{X} - \hat{\mathbf{X}} \right\|_2^2 + \sum_{k=1}^{K} \left\| \mathbf{res}_k - \mathbf{r}_k \right\|_2^2 + \lambda_s \mathcal{L}_{\mathrm{s}}(\mathbf{X}, \hat{\mathbf{X}}), \tag{14}$$

where $\hat{\mathbf{X}}$ are the reconstructed data, $\mathcal{L}_s$ is defined as $\mathcal{L}_s(\mathbf{X}, \hat{\mathbf{X}}) = 1 - \mathrm{SSIM}(\mathbf{X}, \hat{\mathbf{X}})$, denoting the structural similarity index measure to preserve large-scale patterns, and λ_s controls its weight.

AR Pretraining: We pretrain the autoregressive transformer on CMIP6 simulations to learn fundamental climate evolution patterns. At this stage, the model learns to predict the next-scale token maps conditioned on previous tokens and the hybrid-scale prompt. Since the tokenizer discretizes the climate state, we formulate the task as a classification problem, optimizing the cross-entropy loss $\mathcal{L}_{\mathrm{CE}}$ over the codebook indices instead of using pixel-level regression.

AR Fine-tuning: Finally, we fine-tune the pre-trained autoregressive model on the ERA5 and ORAS5 reanalysis datasets to adapt it to real-world forecasting, utilizing the same cross-entropy objective. After fine-tuning, the model performs iterative forecasting by using each single-step forecast as the input for the subsequent time step, enabling seamless extension to long-term forecasts.

5 Experiments

5.1 Experimental Setup

Datasets. We pretrain ClimateAR using historical simulations from the Community Earth System Model version 2 (CESM2) (Danabasoglu et al., 2012), which contributed to the Coupled Model Intercomparison Project Phase 6 (CMIP6) (Eyring et al., 2016b). The training data consist of nine ensemble members spanning 1850–2014, interpolated to a $1° \times 1°$ latitude–longitude grid. Model fine-tuning and evaluation are performed on the ERA5 atmospheric reanalysis and ORAS5 ocean reanalysis datasets (Zuo et al., 2019). The input variables include 4 atmospheric fields at 4 vertical levels, 6 surface variables, and 2 oceanic variables at 6 vertical levels, totaling 34 channels. (See Appendix A.2 for the full variable list.) Missing oceanic values over land are filled with the global mean and masked during training. We use CMIP6 data (1850–2014) for pre-training, ERA5 and ORAS5 (1958–1999) for fine-tuning, 2000–2004 for validation, and 2005–2014 for testing.

Baselines. We evaluate ClimateAR against four leading data-driven methods: Pangu (Bi et al., 2023), GraphCast (Lam et al., 2023), Oneforecast (Gao et al., 2025), and ClimaX (Nguyen et al., 2023). Pangu and ClimaX are based on Vision Transformers (ViT) (Dosovitskiy et al., 2021), while Oneforecast and GraphCast employ graph neural networks. For comparison with conventional physics-based approaches, we include seasonal predictions from the German Meteorological

Service (DWD) (Paxian et al., 2023). The DWD system uses a fully coupled climate model, initialized by nudging atmospheric and oceanic components toward reanalysis states. It produces monthly forecasts with lead times up to six months, evaluated here over the hindcast period 1993–2016. Further baseline details are provided in Appendix A.2.2.

Metrics. To evaluate the forecasting skill on S2I timescales, we use the latitude-weighted Anomalous Correlation Coefficient (ACC) and Root Mean Square Error (RMSE). RMSE measures the absolute deviation in predicted values, providing insight into the overall grid-wise precision. Crucially, the ACC is employed as the **principal metric** for assessing the forecasting skill. It quantifies the spatial and temporal agreement between predicted and observed anomalies—deviations from the long-term climatological mean, thus directly measuring the skill in forecasting meaningful climate variability (e.g., the development of ENSO or blocking events). By focusing on the pattern similarity of anomalies, the ACC is more robust to systematic biases in the mean state than RMSE, as minimizing RMSE tends to make the prediction close to the mean but ignore the anomalies, which is important in climate forecasting.

$$\mathrm{ACC}(\nu) = \sum_{h,w} \frac{\alpha(h)}{HW} \frac{\sum_t \hat{\mathbf{A}}_{\nu,h,w,t} \mathbf{A}_{\nu,h,w,t}}{\sqrt{\sum_t \hat{\mathbf{A}}^2_{\nu,h,w,t} \sum_t \mathbf{A}^2_{\nu,h,w,t}}}, \tag{15}$$

$$\mathrm{RMSE}(\nu) = \sum_{h,w} \frac{\alpha(h)}{HW} \sqrt{\frac{1}{T} \sum_t (\hat{\mathbf{X}}_{\nu,h,w,t} - \mathbf{X}_{\nu,h,w,t})^2}, \tag{16}$$

where $\alpha(h) = H\cos(\lambda_h) / \sum_i \cos(\lambda_i)$ is the latitude weight factor, $\mathbf{X}_{\nu,h,w,t}$ is the ground truth for variable ν at time step t in pixel (h, w) and $\hat{\mathbf{X}}_{\nu,h,w,t}$ is its prediction. The anomaly is $\mathbf{A}_{\nu,h,w,t} = (\mathbf{X}_{\nu,h,w,t} - \mathbf{C}_{\nu,t})$, where $\mathbf{C}_{\nu,t}$ is the climatology (i.e., the mean of variable ν at the time with t in long-term historical periods).

Implementation Details. We configure ClimateAR with a batch size of 64, 8 codebooks with a size of 4096, a hidden dimension of 1024 for both the VQ-VAE and Transformer, 16 heads and 16 layers in the Transformer architecture, and a learning rate of 0.0005 scheduled via linear warmup and cosine annealing. For the baselines, we retrained the model on monthly data with default hyperparameters to adapt to the monthly-scale data prediction task. All these models are trained on 8 NVIDIA A800 80G GPUs. For a fair comparison, all models are pre-trained for a maximum of 50 epochs and fine-tuned for a maximum of 20 epochs with an early stop strategy. More implementation details are provided in Appendix A.2.3.

5.2 Overall Performance

Baseline Comparison. We evaluate ClimateAR against baseline models on 12 key variables spanning multiple pressure levels and surface fields, including geopotential height (z500, z850, z1000), temperature (t2m, t500, t850, t1000), sea surface temperature (sst), precipitation rate (pr), sea level pressure (psl), and surface wind components (u1000, v1000). As summarized in Fig. 2 and detailed in Appendix A.4.1, ClimateAR achieves superior performance across most variables and lead times, with an average ACC improvement of 29.27% over the strongest baseline. More comparison (RMSE comparison in Fig. 8 and low latitude regional forecasting from 1 to 14-month in Fig. 9) can be found in Appendix. A.4.1.This demonstrates the advantage of leveraging high-level, tokenized representations learned from heterogeneous data in guiding climate forecasts.

Notably, ClimateAR exhibits the most significant gains in predicting near-surface temperatures (t2m and t1000)—variables strongly influenced by large-scale climate modes such as ENSO. These results suggest that the model's discrete token-based formulation effectively captures climate-mode dependencies, moving beyond pixel-level regression. While Pangu and ClimaX deliver competitive accuracy through ViT-based global context modeling, their deterministic nature limits their ability to represent systemic climate uncertainty. ClimateAR addresses this by explicitly modeling stochasticity through its autoregressive generative framework.

Visualization. Spatial distributions of ACC for sea surface temperature (Fig. 3) reveal that all models exhibit higher skill in tropical oceans, where climate variability is more predictable. ClimateAR consistently outperforms baselines in these regions, particularly over the tropical Pacific, indicating its enhanced capacity to capture dominant modes of interannual variability. This advantage stems

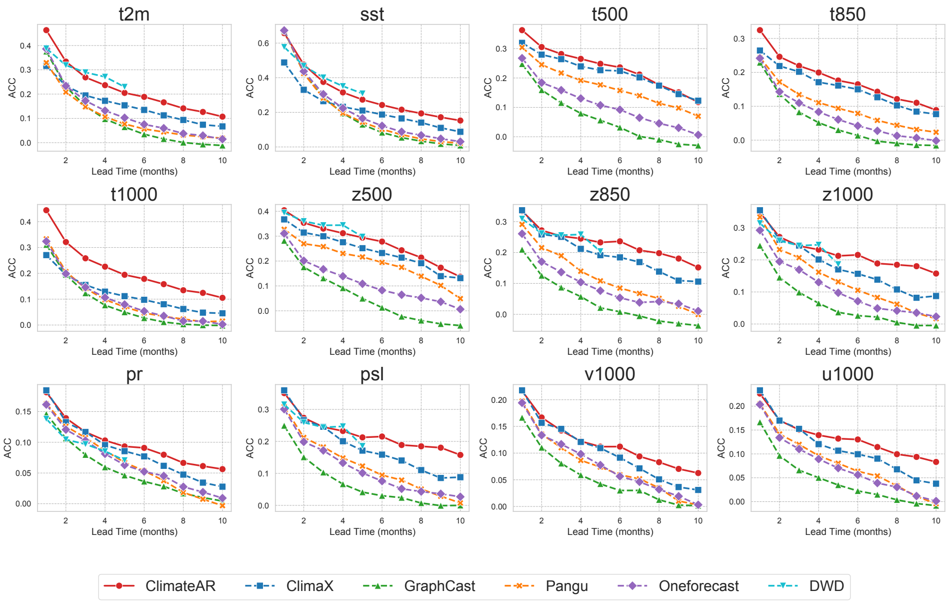

Figure 2: Comparison of ACC for ClimateAR and baselines in the global forecast from 1 to 10-month lead times. More details can be found in Appendix A.4.1.

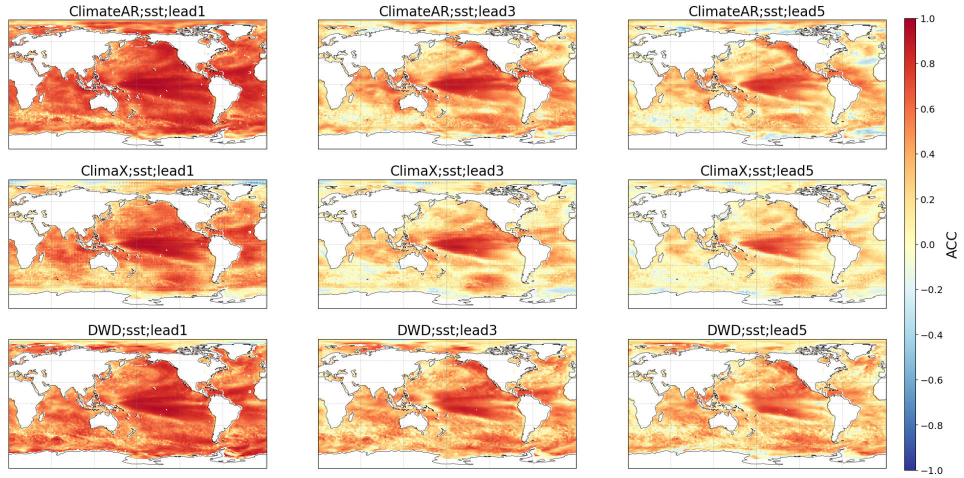

Figure 3: The global ACC distribution of sea surface temperature forecasting with 1-, 3-, and 5-month lead times in the testing set.

from the model's ability to represent spatio-temporal dependencies and uncertainty in a unified generative process. Additional visualizations, including RMSE maps, are provided in Appendix A.4.2.

Zero-shot Forecasting. To evaluate the transferability and generalization capability of ClimateAR, we conduct a zero-shot test on ERA5 data using the pre-trained model trained on the CIMP6 simulated data. From Table 1, we can observe that ClimateAR outperforms all the data-driven models. These results demonstrate its robust transferability and strong generalization performance.

5.3 ENSO Forecasting

For S2I climate forecasting tasks, the El Niño–Southern Oscillation (ENSO) phenomenon is a widely monitored indicator. The performance for ENSO forecasting can be evaluated by the ENSO index calculated by the mean results of t2m in the Niño 3.4 region (170°W to 190°E and 5°S to 5°N). In Fig. 4, we compare the prediction with the observations, which demonstrates that ClimateAR can predict the ENSO index with high accuracy up to 10 months in advance. Specifically, for example, in the test set, a pronounced El Niño event occurred in 2009, and ClimateAR is able to effectively

Table 1: Zero-shot forecasting mean results with lead times of months 1-6 of ClimateAR and data-driven baselines. All the models are only pre-trained on simulated datasets. The best results are bolded, and the second-best results are underlined.

	RMSE (↓)					ACC (↑)				
	ClimateAR	GraphCast	Pangu	Oneforecast	ClimaX	ClimateAR	GraphCast	Pangu	Oneforecast	ClimaX
z500	**35.333**	42.493	41.263	40.663	<u>38.860</u>	**0.323**	0.129	0.240	0.181	<u>0.295</u>
t2m	**2.011**	<u>2.032</u>	2.269	2.032	2.039	**0.276**	0.144	0.134	0.167	<u>0.168</u>
pr($\times 10^{-5}$)	2.037	2.041	**1.986**	2.053	<u>2.003</u>	**0.112**	0.068	0.091	0.088	<u>0.094</u>
psl	**285.299**	306.048	<u>292.689</u>	303.579	301.670	**0.238**	0.094	0.155	0.158	<u>0.205</u>

forecast its onset and decay. In addition, we also compare the ACC between ClimateAR and the baselines for the ENSO index prediction task in Fig. 4. We can observe that ClimateAR outperforms all the baselines, which demonstrates its ability to learn potential climate mode patterns.

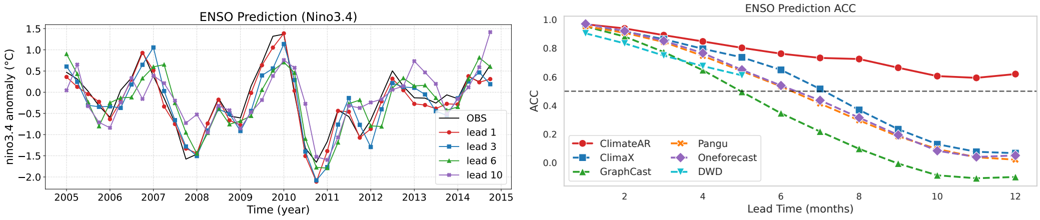

Figure 4: The ENSO index forecast results. The left figure is a comparison of ClimateAR's three-month average ENSO index forecast results and observations at different lead times. The right figure shows the ACC against the forecasting lead time of the ENSO index for ClimateAR and baselines.

5.4 Ensemble Forecasting

Baseline Comparison on Ensemble Forecasting. In Fig. 5, we present Continuous Ranked Probability Score (CRPS) metrics (definition in Appendix. A.3) of 4 key variables for global forecasting tasks. For the deterministic baseline, we obtained different ensemble forecast members through slight perturbations in the initial field. ClimateAR outperforms all baselines with an average CRPS reduction of 23.33%, demonstrating its advantage in probabilistic modeling over the deterministic model.

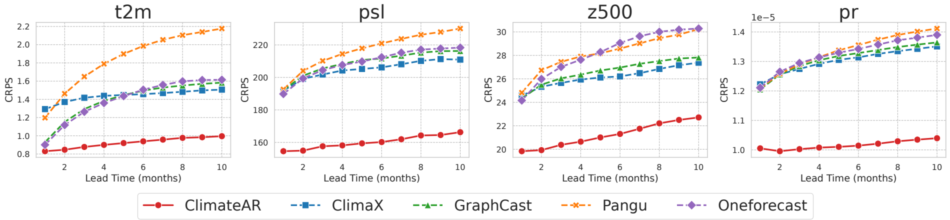

Figure 5: Comparison of CRPS for ClimateAR and baselines in the global forecast from 1 to 10-month lead times. More details can be found in Appendix A.4.1.

Probabilistic Forecasting on ENSO. In Fig. 6, we present the performance of the Probabilistic forecasting on the ENSO index, and we find that: (1) Twice the standard deviation of the ensemble forecast can effectively capture the true observations, proving the effectiveness of climateAR in modeling uncertainties of the climate system. (2) Starting from different time steps, within 12 months, most of the ensemble members of ClimateAR are able to effectively predict the development and dissipation of the ENSO phenomenon, demonstrating its effective capture of climate patterns. In addition, we conduct a power spectral density analysis to show the predicted periodicity characteristics of ENSO in Appendix. A.4.3.

5.5 Decadal Climate Forecasting

To explore the long-term climate simulation potential of ClimateAR, We apply a simple rolling fine-tune procedure (details in Appendix A.5) to mitigates long-term climatology drift and then conduct a decadal forecasting experiment. We initialize the model with the January 1958 climate state

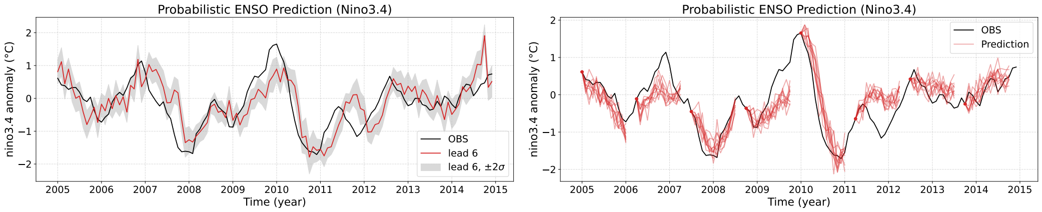

Figure 6: Ensemble forecast results of ENSO index. The left figure compares monthly average forecast results of ClimateAR and observations at 6-month lead time, where the shaded area represents the range indicating twice the ensemble standard deviation. The right figure shows the prediction over 12 months initialized at different start times, including various ensemble forecast members.

and iteratively generate monthly predictions through December 2020, using SST as the only external forcing input. We evaluate the resulting multi-decadal time series by examining the annual and monthly global-mean t2m over 1958–2020 in Fig. 7. ClimateAR produces a stable and physically consistent evolution of global-mean temperature that closely follows the observed long-term trend. This shows that ClimateAR is capable of maintaining coherent large-scale climate statistics over extended periods, highlighting its effectiveness for decadal climate forecasting.

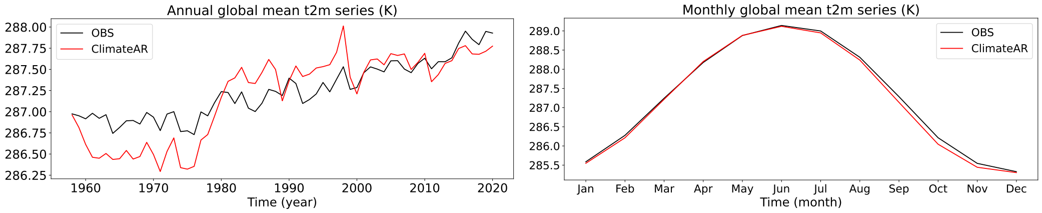

Figure 7: The Global annual-mean and monthly-mean t2m time series of ClimateAR and obversation over 1958–2020.

5.6 Ablation Study

Tokenizer. We design two variants: (1) Removing the cross-domain alignment module (-w/o align) and using a shared network for different data sources. (2) Removing multiple codebooks and not partitioning the feature vector (-w/o part), using a single codebook for vector quantization.

Conditional Control. We design three variants: (1) Removing the hybrid-scale prompt (-w/o hybrid) of token maps. (2) Removing the intra-scale mix tokens (-w/o intra), only using the predicted token as the input to the autoregressive function and using the conditional information as a prefix of token maps. (3) Removing the noise of teach-forcing input (-w/o noise) and using correct tokens as both target and input.

From Table 2 we can find that the lack of any key design will degrade the performance of ClimateAR, which verifies the effectiveness of our proposed methods.

Table 2: Ablation result for the 6 months averaged ACC of ClimateAR.

	ACC (↑)					
		tokenizer		condition		
	ClimateAR	w/o align	w/o part	w/o prompt	w/o intra	w/o noise
z500	**0.331**	0.300	0.282	0.304	0.152	0.296
t2m	**0.285**	0.280	0.267	0.268	0.091	0.257
pr	**0.121**	0.116	0.120	0.107	0.021	0.097
psl	**0.258**	0.236	0.241	0.218	0.061	0.213

6 Conclusions

In this work, we introduce ClimateAR, the first autoregressive probabilistic model for S2I climate forecasting. We introduce novel tokenization and control techniques to extract and utilize high-level features of highly heterogeneous meteorological data for climate forecast generation. Extensive experimental results demonstrate that ClimateAR outperforms all competitive baselines.

7 Ethics statement

As our work only focuses on the weather and climate forecasting problem, there is no potential ethical risk.

8 Reproducibility statement

In the main text, we have formally defined the model architecture with equations. All the implementation details, including dataset descriptions, metrics, and experiment configurations, are provided in the manuscript and the code (available online).

9 Declaration of LLM usage

The author of this paper only used LLM as a grammar checker and simple text polishing tool. LLM was not used in any of the ideas or technical implementations.

References

Dillon J Amaya, Nicola Maher, Clara Deser, Michael G Jacox, Michael A Alexander, Matthew Newman, Juliana Dias, and Jiale Lou. Linking projected changes in seasonal climate predictability and enso amplitude. *Journal of Climate*, 38(3):675–688, 2025.

Paola Arias, Nicolas Bellouin, Erika Coppola, Richard Jones, Gerhard Krinner, Jochem Marotzke, Vaishali Naik, Matthew Palmer, Gian-Kaspar Plattner, Joeri Rogelj, et al. Climate change 2021: the physical science basis. contribution of working group i to the sixth assessment report of the intergovernmental panel on climate change; technical summary. 2021.

Yutong Bai, Xinyang Geng, Karttikeya Mangalam, Amir Bar, Alan L Yuille, Trevor Darrell, Jitendra Malik, and Alexei A Efros. Sequential modeling enables scalable learning for large vision models. In *Proceedings of the IEEE/CVF Conference on Computer Vision and Pattern Recognition*, pp. 22861–22872, 2024.

Kaifeng Bi, Lingxi Xie, Hengheng Zhang, Xin Chen, Xiaotao Gu, and Qi Tian. Accurate medium-range global weather forecasting with 3D neural networks. *Nature*, 619(7970):533–538, 2023.

Cristian Bodnar, Wessel P Bruinsma, Ana Lucic, Megan Stanley, Anna Allen, Johannes Brandstetter, Patrick Garvan, Maik Riechert, Jonathan A Weyn, Haiyu Dong, et al. A foundation model for the earth system. *Nature*, pp. 1–8, 2025.

Boris Bonev, Thorsten Kurth, Christian Hundt, Jaideep Pathak, Maximilian Baust, Karthik Kashinath, and Anima Anandkumar. Spherical fourier neural operators: Learning stable dynamics on the sphere. In *International Conference on Machine Learning*, pp. 2806–2823. PMLR, 2023.

Noah D Brenowitz, Tao Ge, Akshay Subramaniam, Peter Manshausen, Aayush Gupta, David M Hall, Morteza Mardani, Arash Vahdat, Karthik Kashinath, and Michael S Pritchard. Climate in a bottle: Towards a generative foundation model for the kilometer-scale global atmosphere. *arXiv preprint arXiv:2505.06474*, 2025.

Lei Chen, Xiaohui Zhong, Feng Zhang, Yuan Cheng, Yinghui Xu, Yuan Qi, and Hao Li. Fuxi: a cascade machine learning forecasting system for 15-day global weather forecast. *npj climate and atmospheric science*, 6(1):190, 2023a.

Lei Chen, Xiaohui Zhong, Hao Li, Jie Wu, Bo Lu, Deliang Chen, Shang-Ping Xie, Libo Wu, Qingchen Chao, Chensen Lin, et al. A machine learning model that outperforms conventional global subseasonal forecast models. *Nature Communications*, 15(1):6425, 2024.

Mark Chen, Alec Radford, Rewon Child, Jeffrey Wu, Heewoo Jun, David Luan, and Ilya Sutskever. Generative pretraining from pixels. In *International Conference on Machine Learning*, pp. 1691–1703. PMLR, 2020.

Shengchao Chen, Guodong Long, Jing Jiang, Dikai Liu, and Chengqi Zhang. Foundation models for weather and climate data understanding: A comprehensive survey. *arXiv preprint arXiv:2312.03014*, 2023b.

Gokhan Danabasoglu, Susan C Bates, Bruce P Briegleb, Steven R Jayne, Markus Jochum, William G Large, Synte Peacock, and Steve G Yeager. The ccsm4 ocean component. *Journal of Climate*, 25(5):1361–1389, 2012.

Alexey Dosovitskiy, Lucas Beyer, Alexander Kolesnikov, Dirk Weissenborn, Xiaohua Zhai, Thomas Unterthiner, Mostafa Dehghani, Matthias Minderer, Georg Heigold, Sylvain Gelly, Jakob Uszkoreit, and Neil Houlsby. An image is worth 16x16 words: Transformers for image recognition at scale. In *International Conference on Learning Representations*, 2021. URL `https://openreview.net/forum?id=YicbFdNTTy`.

Patrick Esser, Robin Rombach, and Bjorn Ommer. Taming transformers for high-resolution image synthesis. In *Proceedings of the IEEE/CVF conference on Computer Vision and Pattern Recognition*, pp. 12873–12883, 2021.

V. Eyring, P. M. Cox, G. M. Flato, P. J. Gleckler, G. Abramowitz, P. Caldwell, et al. Taking climate model evaluation to the next level. *Nature Climate Change*, 6(9):823–829, 2016a. doi: 10.1038/nclimate3119.

Veronika Eyring, Sandrine Bony, Gerald A Meehl, Catherine A Senior, Bjorn Stevens, Ronald J Stouffer, and Karl E Taylor. Overview of the coupled model intercomparison project phase 6 (cmip6) experimental design and organization. *Geoscientific Model Development*, 9(5):1937–1958, 2016b.

Yuan Gao, Hao Wu, Ruiqi Shu, Huanshuo Dong, Fan Xu, Rui Ray Chen, Yibo Yan, Qingsong Wen, Xuming Hu, Kun Wang, et al. Oneforecast: a universal framework for global and regional weather forecasting. *arXiv preprint arXiv:2502.00338*, 2025.

Zijie Guo, Pumeng Lyu, Fenghua Ling, Lei Bai, Jing-Jia Luo, Niklas Boers, Toshio Yamagata, Takeshi Izumo, Sophie Cravatte, Antonietta Capotondi, et al. Data-driven global ocean modeling for seasonal to decadal prediction. *Science Advances*, 11(33):eadu2488, 2025.

Jian Han, Jinlai Liu, Yi Jiang, Bin Yan, Yuqi Zhang, Zehuan Yuan, Bingyue Peng, and Xiaobing Liu. Infinity: Scaling bitwise autoregressive modeling for high-resolution image synthesis. In *Proceedings of the Computer Vision and Pattern Recognition Conference*, pp. 15733–15744, 2025.

H. Hersbach, B. Bell, P. Berrisford, G. Biavati, A. Horányi, J. Muñoz Sabater, J. Nicolas, C. Peubey, R. Radu, I. Rozum, D. Schepers, A. Simmons, C. Soci, D. Dee, and J-N. Thépaut. The ERA5 global reanalysis: Final results and conclusions. *Quarterly Journal of the Royal Meteorological Society*, 149(753):1783–1834, 2023. doi: 10.1002/qj.4478.

Sebastian Hickman, Ilija Trajković, Julia Kaltenborn, Francis Pelletier, Alexander T Archibald, Yaniv Gurwicz, Peer Nowack, David Rolnick, and Julien Boussard. Causal climate emulation with bayesian filtering. In *The Thirty-ninth Annual Conference on Neural Information Processing Systems*, 2025. URL `https://openreview.net/forum?id=YxPI1c5e09`.

Jordan Hoffmann, Sebastian Borgeaud, Arthur Mensch, Elena Buchatskaya, Trevor Cai, Eliza Rutherford, Diego de Las Casas, Lisa Anne Hendricks, Johannes Welbl, Aidan Clark, et al. Training compute-optimal large language models. *arXiv preprint arXiv:2203.15556*, 2022.

JW Hurrell, MM Holland, PR Gent, S Ghan, JE Kay, PJ Kushner, JF Lamarque, WG Large, D Lawrence, K Lindsay, et al. The community earth system model: A framework for collaborative research, b. am. meteorol. soc., 94, 1339–1360, 2013.

Jessica Hwang, Paulo Orenstein, Judah Cohen, Karl Pfeiffer, and Lester Mackey. Improving subseasonal forecasting in the western us with machine learning. In *Proceedings of the 25th ACM SIGKDD International Conference on Knowledge Discovery & Data Mining*, pp. 2325–2335, 2019.

Jared Kaplan, Sam McCandlish, Tom Henighan, Tom B Brown, Benjamin Chess, Rewon Child, Scott Gray, Alec Radford, Jeffrey Wu, and Dario Amodei. Scaling laws for neural language models. *arXiv preprint arXiv:2001.08361*, 2020.

Remi Lam, Alvaro Sanchez-Gonzalez, Matthew Willson, Peter Wirnsberger, Meire Fortunato, Ferran Alet, Suman Ravuri, Timo Ewalds, Zach Eaton-Rosen, Weihua Hu, et al. Learning skillful medium-range global weather forecasting. *Science*, 382(6677):1416–1421, 2023.

Doyup Lee, Chiheon Kim, Saehoon Kim, Minsu Cho, and Wook-Shin Han. Autoregressive image generation using residual quantization. In *Proceedings of the IEEE/CVF conference on Computer Vision and Pattern Recognition*, pp. 11523–11532, 2022.

Tianhong Li, Yonglong Tian, He Li, Mingyang Deng, and Kaiming He. Autoregressive image generation without vector quantization. *Advances in Neural Information Processing Systems*, 37: 56424–56445, 2024.

Yang Liu, Zinan Zheng, Jiashun Cheng, Fugee Tsung, Deli Zhao, Yu Rong, and Jia Li. Cirt: Global subseasonal-to-seasonal forecasting with geometry-inspired transformer. *arXiv preprint arXiv:2502.19750*, 2025.

Ignacio Lopez-Gomez, Zhong Yi Wan, Leonardo Zepeda-Núñez, Tapio Schneider, John Anderson, and Fei Sha. Dynamical-generative downscaling of climate model ensembles. *Proceedings of the National Academy of Sciences*, 122(17):e2420288122, 2025.

Jiasen Lu, Christopher Clark, Rowan Zellers, Roozbeh Mottaghi, and Aniruddha Kembhavi. UNIFIED-IO: A unified model for vision, language, and multi-modal tasks. In *The Eleventh International Conference on Learning Representations*, 2023.

Gerald A Meehl, Jadwiga H Richter, Haiyan Teng, Antonietta Capotondi, Kim Cobb, Francisco Doblas-Reyes, Markus G Donat, Matthew H England, John C Fyfe, Weiqing Han, et al. Initialized earth system prediction from subseasonal to decadal timescales. *Nature Reviews Earth & Environment*, 2(5):340–357, 2021.

Tung Nguyen, Johannes Brandstetter, Ashish Kapoor, Jayesh K Gupta, and Aditya Grover. Climax: a foundation model for weather and climate. In *Proceedings of International Conference on Machine Learning*, pp. 25904–25938, 2023.

Joel Oskarsson, Tomas Landelius, Marc Deisenroth, and Fredrik Lindsten. Probabilistic weather forecasting with hierarchical graph neural networks. *Advances in Neural Information Processing Systems*, 37:41577–41648, 2024.

Yatian Pang, Peng Jin, Shuo Yang, Bin Lin, Bin Zhu, Zhenyu Tang, Liuhan Chen, Francis EH Tay, Ser-Nam Lim, Harry Yang, et al. Next patch prediction for autoregressive visual generation. *arXiv preprint arXiv:2412.15321*, 2024.

A Paxian, B Mannig, M Tivig, K Reinhardt, K Isensee, Alexander Pasternack, A Hoff, K Pankatz, S Buchholz, and S Wehring. The dwd climate predictions website: Towards a seamless outlook based on subseasonal, seasonal and decadal predictions. *Climate Services*, 30, 2023.

Ilan Price, Alvaro Sanchez-Gonzalez, Ferran Alet, Tom R Andersson, Andrew El-Kadi, Dominic Masters, Timo Ewalds, Jacklynn Stott, Shakir Mohamed, Peter Battaglia, et al. Probabilistic weather forecasting with machine learning. *Nature*, 637(8044):84–90, 2025.

Alec Radford, Jeffrey Wu, Rewon Child, David Luan, Dario Amodei, Ilya Sutskever, et al. Language models are unsupervised multitask learners. *OpenAI blog*, 1(8):9, 2019.

Neelesh Rampal, Peter B Gibson, Steven Sherwood, Gab Abramowitz, and Sanaa Hobeichi. A reliable generative adversarial network approach for climate downscaling and weather generation. *Authorea Preprints*, 2024.

Suman Ravuri, Karel Lenc, Matthew Willson, Dmitry Kangin, Remi Lam, Piotr Mirowski, Megan Fitzsimons, Maria Athanassiadou, Sheleem Kashem, Sam Madge, et al. Skilful precipitation nowcasting using deep generative models of radar. *Nature*, 597(7878):672–677, 2021.

Xiaoli Ren, Xiaoyong Li, Kaijun Ren, Junqiang Song, Zichen Xu, Kefeng Deng, and Xiang Wang. Deep learning-based weather prediction: a survey. *Big Data Research*, 23:100178, 2021.

Jian Sha, Xinyu Chen, Yaxin Chang, Man Zhang, and Xue Li. A spatial weather generator based on conditional deep convolution generative adversarial nets (cdcgan). *Climate Dynamics*, 62(2): 1275–1290, 2024.

Jimeng Shi, Azam Shirali, Bowen Jin, Sizhe Zhou, Wei Hu, Rahuul Rangaraj, Shaowen Wang, Jiawei Han, Zhaonan Wang, Upmanu Lall, et al. Deep learning and foundation models for weather prediction: A survey. *arXiv preprint arXiv:2501.06907*, 2025.

Keyu Tian, Yi Jiang, Zehuan Yuan, Bingyue Peng, and Liwei Wang. Visual autoregressive modeling: Scalable image generation via next-scale prediction. *Advances in neural information processing systems*, 37:84839–84865, 2024.

Kevin E Trenberth, B Hoskins, P Jones, T Karl, P Ambenje, B Jallow, R Bojariu, D Easterling, A Tank, D Parker, et al. Observations: surface and atmospheric climate change. *NCAR Report*, 2007.

Aaron Van den Oord, Nal Kalchbrenner, Lasse Espeholt, Oriol Vinyals, Alex Graves, et al. Conditional image generation with pixelcnn decoders. *Advances in neural information processing systems*, 29, 2016.

Aäron Van Den Oord, Nal Kalchbrenner, and Koray Kavukcuoglu. Pixel recurrent neural networks. In *International Conference on Machine Learning*, pp. 1747–1756. PMLR, 2016.

Yogesh Verma, Markus Heinonen, and Vikas Garg. Climode: Climate and weather forecasting with physics-informed neural odes. In *International Conference on Learning Representations*. International Conference on Learning Representations, 2024.

Jing Xiong, Gongye Liu, Lun Huang, Chengyue Wu, Taiqiang Wu, Yao Mu, Yuan Yao, Hui Shen, Zhongwei Wan, Jinfa Huang, et al. Autoregressive models in vision: A survey. *arXiv preprint arXiv:2411.05902*, 2024.

Wanghan Xu, Fenghua Ling, Tao Han, Hao Chen, Wanli Ouyang, and LEI BAI. Generalizing weather forecast to fine-grained temporal scales via physics-ai hybrid modeling. *Advances in Neural Information Processing Systems*, 37:23325–23351, 2024.

Lili Yu, Bowen Shi, Ramakanth Pasunuru, Benjamin Muller, Olga Golovneva, Tianlu Wang, Arun Babu, Binh Tang, Brian Karrer, Shelly Sheynin, et al. Scaling autoregressive multi-modal models: Pretraining and instruction tuning. *arXiv preprint arXiv:2309.02591*, 2023.

Fuqing Zhang, Y Qiang Sun, Linus Magnusson, Roberto Buizza, Shian-Jiann Lin, Jan-Huey Chen, and Kerry Emanuel. What is the predictability limit of midlatitude weather? *Journal of the Atmospheric Sciences*, 76(4):1077–1091, 2019.

Yuchen Zhang, Mingsheng Long, Kaiyuan Chen, Lanxiang Xing, Ronghua Jin, Michael I Jordan, and Jianmin Wang. Skilful nowcasting of extreme precipitation with nowcastnet. *Nature*, 619 (7970):526–532, 2023.

Hao Zuo, Magdalena Alonso Balmaseda, Steffen Tietsche, Kristian Mogensen, and Michael Mayer. The ecmwf operational ensemble reanalysis–analysis system for ocean and sea ice: a description of the system and assessment. *Ocean science*, 15(3):779–808, 2019.

A Appendix

A.1 Additional Method Details

Tokenizer alignment and partition. For our multi-scale VQ tokenizer implementation, we incorporate two key technical components in the tokenizer pre-training procedure: partition with multi-codebook matching and labeled cross-domain data alignment. The detailed implementation algorithm is presented in Alg.1.

Algorithm 1 Aligned tokenizer and partition.

```
Input: Input raw data $\mathbf{X}$, label of data source $l$, scale $K$, partitions $N$
  Selection by label: $\mathbf{X}_l = \mathrm{CNN}_l(\mathbf{X})$
  $\mathbf{f} = \varepsilon(\mathbf{X}_l)$
  Initialize: $\hat{\mathbf{f}} = 0$
  for $k = 1$ to $K$ do
    $\mathbf{res}_k = (\mathrm{down}(\mathbf{f}, (h_w, h_k)))$
    $[\mathbf{res}_k^{(1)}, \mathbf{res}_k^{(2)}, \ldots, \mathbf{res}_k^{(N)}]$ = $\mathbf{res}_k$
    for $i = 1$ to $N$ do
      $\mathbf{r}_k^{(i)} = \mathrm{look\_up}(\mathbf{res}_k^{(i)})$
    end for
    $\mathbf{r}_k$ = $[\mathbf{r}_k^{(1)}, \mathbf{r}_k^{(2)}, \ldots, \mathbf{r}_k^{(N)}]$
    $\mathbf{f} = \mathbf{f} - \mathrm{up}(\mathbf{r}_k, (h, w))$
    $\hat{\mathbf{f}} = \hat{\mathbf{f}} + \mathrm{up}(\mathbf{r}_k, (h, w))$
    $\hat{\mathbf{f}}_k = \hat{\mathbf{f}}$
  end for
  $\hat{\mathbf{X}}_l = \mathcal{D}(\hat{\mathbf{f}})$
  Selection by label: $\hat{\mathbf{X}} = \mathrm{CNN}_l(\hat{\mathbf{X}}_l)$
  return $\hat{\mathbf{X}}$
```

Noise Injection. Furthermore, we introduce noise during the training phase of the autoregressive (AR) model to alleviate exposure bias inherent in autoregressive architectures. The whole process is illustrated in Alg.2.

Algorithm 2 Tokenize data with noise.

```
Input: Input feature map $\mathbf{f}$, scale $K$, noise rate $p$
  Initialize: target token maps $\mathbf{r}_{tgt} = []$, teach-forcing input token_maps $\mathbf{r}_{in} = []$.
  for $k = 1$ to $K$ do
    $\mathbf{r}_k = \mathrm{Quantize}(\mathbf{f})$
    $\mathbf{r}_{tgt} = \mathbf{r}_{tgt} \cup \{\mathbf{r}_k\}$
    $\mathbf{r}_k^{\mathrm{noisy}} = \mathrm{Random\_Replace}(\mathbf{r}_k, p)$
    $\mathbf{r}_{tgt} = \mathbf{r}_{tgt} \cup \{\mathbf{r}_k^{\mathrm{noisy}}\}$
    $\mathbf{f} = \mathbf{f} - \mathrm{up}(\mathbf{r}_k, (h, w))$
  end for
  return $\mathbf{r}_{tgt}, \mathbf{r}_{in}$
```

A.2 Additional Experimental Details

A.2.1 Datasets

CMIP6 datasets. We use historical simulations from the Community Earth System Model version 2 (CESM2), developed by the National Center for Atmospheric Research (NCAR) (Danabasoglu et al., 2012), which participated in the Coupled Model Intercomparison Project Phase 6 (CMIP6) (Eyring et al., 2016). The CESM2 historical simulations comprise 9 ensemble realizations with different initial conditions, covering 1850–2014, which form 9 simulated datasets used for our model pre-training. All fields were interpolated onto a $1^\circ \times 1^\circ$ grid using bilinear interpolation.

ERA5 datasets. The ERA5 dataset is the fifth-generation reanalysis product from the European Centre for Medium-Range Weather Forecasts (ECMWF). ERA5 provides hourly estimates of atmospheric, land, and oceanic climate variables. The data cover the Earth on a 30-kilometer grid and resolve the atmosphere using 137 vertical levels from the surface to an altitude of 80 kilometers. We used the period from 1958 to 2014 for model training. All fields were interpolated onto a $1^\circ \times 1^\circ$ grid using bilinear interpolation.

ORAS5 datasets. The ORAS5 dataset is the reanalysis product of the ECMWF OCEAN5 system, which is a new global eddy-permitting ocean-sea ice ensemble reanalysis system. ORAS5 provides ocean state estimates from 1979 to the present and extends historical records back to 1958, assimilating temperature and salinity in-situ observations as well as sea ice concentration data. We used the period from 1958 to 2014 for model training. All fields were interpolated onto a 1° × 1° grid using bilinear interpolation.

Variables. Table 3 presents all the variables we use in experiments, including 4 atmospheric variables at 4 vertical levels, 6 single-level variables, and 2 oceanic variables at 6 vertical levels, totaling 34 variables. For sea surface temperature (sst), we use 5-meter sea temperature as an approximation in the corresponding tests.

Table 3: Variables used in experiments.

Type	Varibale name	Abbreviation	Levels or Depth
Atmospheric	geopotential	z	200hPa,500hPa,850hPa,1000hPa
Atmospheric	u wind component	u	200hPa,500hPa,850hPa,1000hPa
Atmospheric	v wind component	v	200hPa,500hPa,850hPa,1000hPa
Atmospheric	temperature	t	200hPa,500hPa,850hPa,1000hPa
Ocean	salinity	so	5m,20m,40m,90m,200m,300m
Ocean	sea temperature	temp	5m,20m,40m,90m,200m,300m
Single	2 metre temperature	t2m	
Single	u wind stress component	tauu	
Single	v wind stress component	tauv	
Single	precipitation rate	pr	
Single	sea level pressure	psl	
Single	Sea Surface Height	zos	

A.2.2 BASELINES

Pangu. Pangu is a Vision Transformer-based data-driven model with three-dimensional deep networks equipped with Earth-specific priors. Pangu processes pressure layer variables using 3D patches and single-layer variables using 2D patches, then aggregates the two to perform prediction tasks.

GraphCast. GraphCast is a Graph Neural Network-based data-driven model. GraphCast uses multi-mesh method to construct the graph and apply a stage with an encoder, processor, and decoder to learn the complex dynamics of the system.

Oneforecast. Oneforecast is a Graph Neural Network-based data-driven model. Oneforecast constructs a multi-scale graph structure and introduces an adaptive messaging mechanism with dynamic gating units for more accurate forecasting.

ClimaX. A Vision Transformer-based data-driven foundation model for weather and climate forecasting, which tokenizes variables independently and uses an aggregation module to model the dependency between variables.

DWD. We employ seasonal climate forecasts from the German Meteorological Service. The German Meteorological Service forecasting system is based on a fully coupled climate model. Its initialization is achieved by nudging the model's atmospheric and oceanic components toward reanalysis data. The system produces monthly forecasts with a lead time of up to six months, and its hindcast period spans 1993–2016. These datasets are available through the Copernicus Climate Change Service (C3S) hosted by the European Centre for Medium-Range Weather Forecasts (ECMWF).

A.2.3 ADDITIONAL IMPLEMENTATION DETAILS

ClimateAR. In the Table 4, we present the detailed hyperparameter settings of ClimateAR. In addition, our model generates multiple forecast ensemble members through probabilistic sampling over multiple steps, and we ultimately use the average of 200 members as the final forecast result.

Table 4: The detailed hyperparameter settings of ClimateAR

Hyperparameter	Tokenizer	Hyperparameter	AR Transformer
dropout	0	dropout	0
learning rate (lr)	$5e-4$	pre-train learning rate (lr_p)	$5e-4$
batch size (B)	128	pre-train batch size (B_p)	64
hidden dimension (d)	1024	hidden dimension (d)	1024
codebooks dimension (c)	128	noise rate (p)	0.3
number of codebooks (N)	8	transformer heads (h)	16
size of codebooks (V)	4096	transformer layers (l)	16
number of scales (K)	10	number of scales (K)	10
loss function weight (λ_s)	1	fine-tune learning rate (lr_t)	$5e-5$
		fine-tune batch size (B_t)	64
		prompt length (L)	256

Data-driven baselines. For Pangu, Oneforecast, and GraphCast, we utilized the source code of Oneforecast from `https://github.com/YuanGao-YG/OneForecast`, retraining the model with all default hyperparameters on monthly averaged data and conducting evaluations. For ClimaX, we adopted the publicly available source code from `https://github.com/microsoft/ClimaX`, retraining and evaluating it using the same hyperparameters with 1.40625° × 1.40625° (patch size with 4×4).

A.3 Continuous Ranked Probability Score

The detailed definition of metric CRPS is as follows:

$$\begin{aligned} \operatorname{CRPS}\left(F, x_{\text{obs}}\right) &= \int_{-\infty}^{\infty}\left(F(x)-\mathrm{H}\left(x-x_{\text{obs}}\right)\right)^{2} dx \\ H(s) &= \begin{cases} 0 & s<0 \\ 1 & s \geq 0 \end{cases} \end{aligned} \tag{17}$$

where F is the cumulative distribution function (CDF) of the prediction x, H is the Heaviside function and denotes the CDF of the observation x_{obs}. Then we can compute the global average CRPS using latitude-weighted averaging.

$$\operatorname{CRPS}(\nu) = \sum_{h,w} \frac{\alpha(h)}{THW} \sum_{t} \operatorname{CRPS}(\mathbf{F}_{\nu,h,w,t}, \mathbf{X}_{\nu,h,w,t}) \tag{18}$$

where $\alpha(h) = H\cos(\lambda_h)/\sum_i \cos(\lambda_i)$ is the latitude weight factor, $\mathbf{X}_{\nu,h,w,t}$ is the ground truth for variable ν at time step t in pixel (h, w) and $\mathbf{F}_{\nu,h,w,t}$ is the CDF of its prediction.

A.4 Additional Results

A.4.1 Comparison with Baselines

Comparison on RMSE. In Fig. 8, we give the comparison of RMSE for ClimateAR and baselines in the global forecast across 1- to 10-month lead times. The full results demonstrate that even though ClimateAR does not rely on pixel-wise MSE loss and only learns token-level classification in a high-level feature space, it still achieves the lowest RMSE prediction error in most cases, proving the effectiveness of modeling systematic uncertainty and spatiotemporal multi-scale dependencies in long-term forecasting tasks.

Full result. In Table 5, 6, we present all detailed metrics of the key variables for the global forecasting tasks.

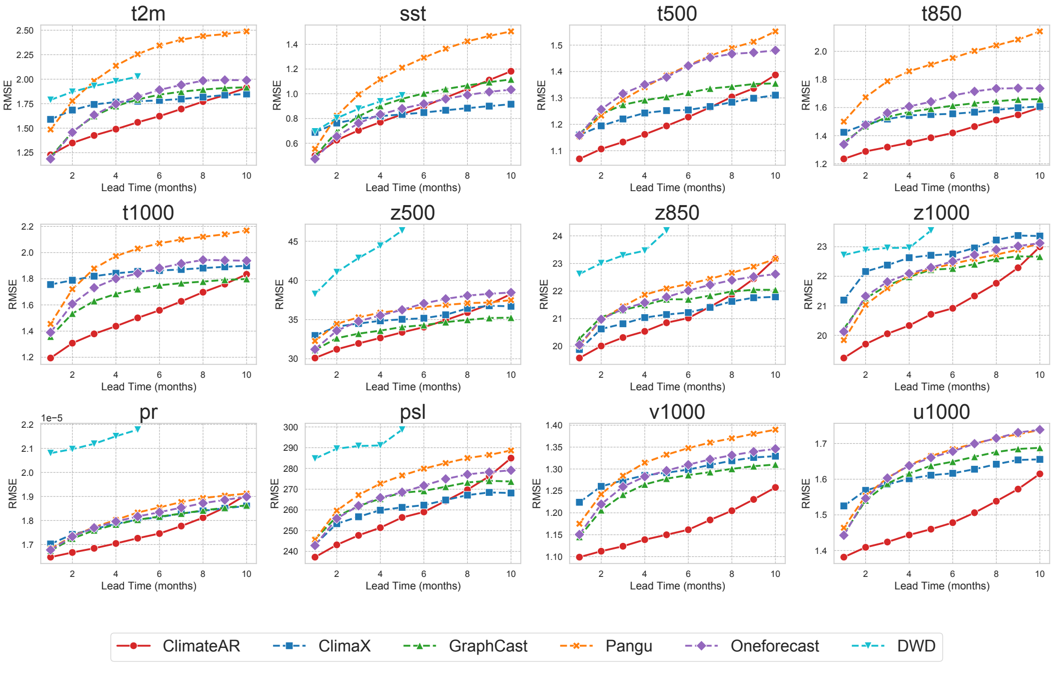

Figure 8: Comparison of RMSE for ClimateAR and baselines in the global forecast across 1- to 10-month lead times

Table 5: Global forecasting CRPS of ClimateAR and baselines. The best results are bolded.

		CRPS (↓)							CRPS (↓)				
var	lead	ClimateAR	GraphCast	Pangu	Oneforecast	ClimaX	var	lead	ClimateAR	GraphCast	Pangu	Oneforecast	ClimaX
t2m	1	**0.831**	0.929	1.198	0.901	1.293	pr	1	**1.01E-05**	1.21E-05	1.21E-05	1.21E-05	1.22E-05
	2	**0.847**	1.152	1.463	1.118	1.371		2	**9.96E-06**	1.26E-05	1.26E-05	1.27E-05	1.26E-05
	3	**0.878**	1.293	1.650	1.263	1.418		3	**1.00E-05**	1.28E-05	1.29E-05	1.29E-05	1.27E-05
	4	**0.900**	1.383	1.790	1.360	1.439		4	**1.01E-05**	1.30E-05	1.31E-05	1.31E-05	1.29E-05
	5	**0.920**	1.447	1.899	1.436	1.448		5	**1.01E-05**	1.32E-05	1.34E-05	1.33E-05	1.31E-05
	6	**0.939**	1.496	1.986	1.506	1.457		6	**1.01E-05**	1.33E-05	1.36E-05	1.34E-05	1.31E-05
	7	**0.958**	1.529	2.054	1.558	1.469		7	**1.02E-05**	1.34E-05	1.37E-05	1.36E-05	1.33E-05
	8	**0.977**	1.552	2.104	1.598	1.483		8	**1.03E-05**	1.35E-05	1.39E-05	1.37E-05	1.33E-05
	9	**0.984**	1.570	2.140	1.612	1.498		9	**1.03E-05**	1.36E-05	1.40E-05	1.38E-05	1.34E-05
	10	**0.996**	1.583	2.177	1.615	1.507		10	**1.04E-05**	1.36E-05	1.41E-05	1.39E-05	1.35E-05
	11	**0.999**	1.596	2.226	1.620	1.507		11	**1.04E-05**	1.37E-05	1.42E-05	1.40E-05	1.36E-05
	12	**1.004**	1.615	2.284	1.633	1.505		12	**1.04E-05**	1.37E-05	1.43E-05	1.40E-05	1.36E-05
psl	1	**154.569**	192.223	192.649	189.818	191.848	z500	1	**19.833**	24.322	24.825	24.160	24.566
	2	**154.931**	201.041	204.039	199.346	199.155		2	**19.926**	25.503	26.731	25.988	25.328
	3	**157.615**	205.517	210.173	204.485	201.779		3	**20.377**	26.042	27.453	27.019	25.655
	4	**158.154**	208.316	214.462	207.659	204.259		4	**20.646**	26.359	27.906	27.630	25.941
	5	**159.407**	210.686	217.911	209.790	205.218		5	**21.007**	26.713	28.175	28.275	26.113
	6	**160.212**	211.672	220.934	212.426	206.170		6	**21.305**	26.960	28.580	29.056	26.205
	7	**161.927**	213.378	223.726	215.205	208.116		7	**21.748**	27.283	29.026	29.632	26.484
	8	**164.266**	215.256	226.267	217.126	210.184		8	**22.209**	27.514	29.468	30.007	26.844
	9	**164.532**	216.191	227.955	217.776	211.274		9	**22.499**	27.733	29.770	30.190	27.163
	10	**166.283**	216.270	230.086	218.335	210.944		10	**22.712**	27.818	30.237	30.287	27.377
	11	**165.951**	216.072	232.161	219.141	211.645		11	**22.756**	27.840	30.860	30.343	27.565
	12	**165.857**	216.629	232.499	218.666	211.306		12	**22.776**	27.929	31.294	30.365	27.588

Table 6: Global forecasting detail results of ClimateAR and baselines. The best results are bolded, and the second best results are underlined.

		RMSE (↓)						ACC (↑)					
var	lead	ClimateAR	Pangu	GraphCast	Oneforecast	ClimaX	DWD	ClimateAR	Pangu	GraphCast	Oneforecast	ClimaX	DWD
t2m	1	1.228	1.487	1.204	**1.187**	1.590	1.789	**0.463**	0.329	0.376	0.386	0.316	0.388
	2	**1.349**	1.777	1.462	1.457	1.685	1.871	**0.334**	0.208	0.230	0.234	0.234	0.319
	3	**1.426**	1.982	1.624	1.635	1.743	1.930	0.269	0.148	0.150	0.172	0.195	**0.289**
	4	**1.490**	2.137	1.726	1.747	1.767	1.978	0.237	0.107	0.097	0.132	0.172	**0.271**
	5	**1.560**	2.256	1.793	1.823	1.775	2.026	0.205	0.077	0.064	0.103	0.154	**0.230**
	6	**1.622**	2.344	1.842	1.891	1.784	-	**0.189**	0.056	0.035	0.075	0.135	-
	7	**1.696**	2.403	1.872	1.942	1.798	-	**0.166**	0.044	0.015	0.060	0.112	-
	8	**1.771**	2.440	1.894	1.985	1.817	-	**0.141**	0.031	0.001	0.037	0.094	-
	9	**1.837**	2.460	1.910	1.992	1.839	-	**0.126**	0.024	-0.007	0.029	0.074	-
	10	1.913	2.488	1.918	1.990	**1.849**	-	**0.107**	0.018	-0.012	0.014	0.067	-
sst	1	0.500	0.554	0.495	**0.473**	0.688	0.695	0.657	**0.675**	0.671	0.673	0.488	0.577
	2	**0.625**	0.823	0.693	0.654	0.763	0.803	**0.476**	0.425	0.427	0.437	0.330	0.469
	3	**0.704**	0.994	0.818	0.762	0.798	0.879	0.376	0.282	0.286	0.305	0.264	**0.401**
	4	**0.771**	1.117	0.902	0.833	0.819	0.938	0.315	0.195	0.194	0.224	0.232	**0.351**
	5	**0.833**	1.211	0.959	0.880	**0.833**	0.987	0.273	0.143	0.130	0.165	0.210	**0.309**
	6	0.898	1.292	1.003	0.919	**0.848**	-	**0.242**	0.102	0.083	0.122	0.187	-
	7	0.968	1.365	1.038	0.958	**0.867**	-	**0.215**	0.071	0.054	0.088	0.165	-
	8	1.039	1.424	1.067	0.990	**0.884**	-	**0.194**	0.047	0.034	0.068	0.141	-
	9	1.111	1.468	1.094	1.016	**0.900**	-	**0.172**	0.031	0.018	0.048	0.110	-
	10	1.182	1.505	1.116	1.033	**0.916**	-	**0.153**	0.022	0.009	0.031	0.088	-
t500	1	**1.069**	1.154	1.164	1.158	1.160	-	**0.363**	0.304	0.248	0.268	0.320	-
	2	**1.107**	1.233	1.239	1.256	1.194	-	**0.305**	0.245	0.159	0.184	0.279	-
	3	**1.133**	1.293	1.274	1.316	1.220	-	**0.282**	0.217	0.115	0.159	0.264	-
	4	**1.162**	1.341	1.291	1.351	1.243	-	**0.265**	0.192	0.080	0.130	0.239	-
	5	**1.194**	1.385	1.304	1.378	1.252	-	**0.248**	0.177	0.056	0.107	0.227	-
	6	**1.228**	1.423	1.320	1.422	1.254	-	**0.236**	0.158	0.032	0.092	0.224	-
	7	**1.264**	1.460	1.335	1.453	1.267	-	**0.212**	0.140	0.001	0.065	0.202	-
	8	1.304	1.489	1.343	1.467	**1.284**	-	**0.177**	0.114	-0.010	0.046	0.174	-
	9	1.336	1.513	1.353	1.472	**1.299**	-	**0.151**	0.098	-0.025	0.030	0.145	-
	10	1.387	1.552	1.355	1.480	**1.310**	-	0.118	0.070	-0.030	0.006	**0.123**	-
t850	1	**1.235**	1.500	1.352	1.338	1.424	-	**0.324**	0.244	0.229	0.242	0.264	-
	2	**1.288**	1.673	1.468	1.477	1.481	-	**0.246**	0.172	0.136	0.143	0.219	-
	3	**1.319**	1.787	1.533	1.562	1.518	-	**0.219**	0.134	0.083	0.110	0.202	-
	4	**1.350**	1.858	1.569	1.608	1.544	-	**0.200**	0.111	0.052	0.083	0.171	-
	5	**1.385**	1.906	1.592	1.641	1.550	-	**0.176**	0.094	0.030	0.061	0.161	-
	6	**1.419**	1.952	1.614	1.686	1.555	-	**0.165**	0.079	0.014	0.042	0.150	-
	7	**1.465**	2.003	1.631	1.715	1.567	-	**0.143**	0.058	-0.003	0.028	0.127	-
	8	**1.511**	2.042	1.645	1.735	1.583	-	**0.121**	0.044	-0.009	0.013	0.103	-
	9	**1.548**	2.083	1.657	1.738	1.599	-	**0.110**	0.031	-0.014	0.007	0.084	-
	10	**1.600**	2.142	1.660	1.736	1.608	-	**0.089**	0.023	-0.016	-0.002	0.077	-
t1000	1	**1.194**	1.455	1.358	1.390	1.756	-	**0.444**	0.333	0.310	0.324	0.271	-
	2	**1.308**	1.720	1.534	1.608	1.789	-	**0.321**	0.207	0.194	0.199	0.194	-
	3	**1.379**	1.878	1.630	1.731	1.820	-	**0.258**	0.142	0.123	0.146	0.155	-
	4	**1.438**	1.973	1.684	1.800	1.842	-	**0.226**	0.098	0.077	0.106	0.129	-
	5	**1.501**	2.031	1.721	1.841	1.856	-	**0.194**	0.070	0.050	0.080	0.112	-
	6	**1.559**	2.070	1.750	1.882	1.863	-	**0.179**	0.047	0.027	0.054	0.098	-
	7	**1.627**	2.100	1.766	1.916	1.871	-	**0.158**	0.033	0.012	0.035	0.080	-
	8	**1.697**	2.121	1.778	1.944	1.882	-	**0.135**	0.023	0.003	0.015	0.062	-
	9	**1.759**	2.140	1.791	1.941	1.891	-	**0.124**	0.013	0.000	0.015	0.048	-
	10	1.834	2.168	**1.798**	1.938	1.899	-	**0.105**	0.015	-0.002	0.003	0.045	-
z500	1	**30.096**	32.268	31.120	31.201	32.974	38.268	**0.404**	0.327	0.282	0.311	0.367	0.394
	2	**31.209**	34.459	32.624	33.584	34.104	41.048	0.354	0.270	0.176	0.201	0.315	**0.360**
	3	**31.956**	35.288	33.206	34.789	34.498	42.861	0.330	0.258	0.131	0.167	0.300	**0.344**
	4	**32.661**	35.886	33.592	35.531	34.841	44.424	0.312	0.231	0.091	0.139	0.276	**0.344**
	5	**33.372**	36.229	34.053	36.249	35.038	46.368	0.294	0.216	0.049	0.108	0.252	**0.298**
	6	**34.033**	36.584	34.297	37.064	35.172	-	**0.278**	0.194	0.013	0.083	0.232	-
	7	34.935	36.871	**34.674**	37.643	35.609	-	**0.243**	0.175	-0.023	0.064	0.214	-
	8	35.895	37.095	**34.962**	38.062	36.429	-	**0.214**	0.139	-0.039	0.052	0.191	-
	9	36.937	37.189	**35.200**	38.288	36.767	-	**0.173**	0.102	-0.053	0.036	0.139	-
	10	38.270	37.485	**35.244**	38.458	36.701	-	**0.137**	0.049	-0.059	0.006	0.131	-
z850	1	**19.573**	20.017	20.271	20.052	19.881	22.619	0.334	0.291	0.210	0.261	**0.337**	0.309
	2	**20.009**	20.961	21.053	20.978	20.626	23.007	**0.272**	0.216	0.125	0.170	0.259	0.262
	3	**20.315**	21.443	21.316	21.353	20.814	23.292	0.253	0.190	0.087	0.137	0.251	**0.256**
	4	**20.540**	21.867	21.497	21.579	21.039	23.462	0.245	0.139	0.057	0.104	0.212	**0.258**
	5	**20.851**	22.093	21.702	21.784	21.150	24.194	**0.233**	0.108	0.021	0.076	0.191	0.204
	6	**21.021**	22.258	21.698	22.015	21.220	-	**0.236**	0.085	0.008	0.054	0.184	-
	7	21.431	22.442	21.835	22.225	**21.407**	-	**0.207**	0.068	-0.005	0.038	0.169	-

Continued on next page

Continued

	8	21.872	22.662	21.983	22.395	**21.625**	-	**0.198**	0.051	-0.022	0.041	0.138	-
	9	22.445	22.885	22.046	22.520	**21.758**	-	**0.180**	0.026	-0.029	0.034	0.109	-
	10	23.183	23.168	22.044	22.614	**21.789**	-	**0.152**	-0.001	-0.036	0.011	0.106	-
z1000	1	**19.232**	19.839	20.222	20.125	21.193	22.719	0.348	0.334	0.245	0.293	**0.355**	0.314
	2	**19.703**	21.033	21.251	21.326	22.161	22.891	**0.272**	0.232	0.145	0.195	0.263	0.260
	3	**20.054**	21.594	21.692	21.811	22.378	22.960	0.243	0.207	0.099	0.169	**0.245**	0.244
	4	**20.331**	22.029	21.979	22.094	22.629	22.963	0.232	0.162	0.065	0.130	0.201	**0.247**
	5	**20.712**	22.256	22.220	22.296	22.711	23.549	**0.213**	0.132	0.036	0.097	0.170	0.186
	6	**20.916**	22.422	22.262	22.505	22.751	-	**0.216**	0.105	0.026	0.071	0.157	-
	7	**21.333**	22.589	22.407	22.725	22.959	-	**0.189**	0.083	0.022	0.049	0.138	-
	8	**21.764**	22.734	22.588	22.903	23.227	-	**0.185**	0.062	0.005	0.041	0.108	-
	9	**22.289**	22.899	22.674	23.021	23.379	-	**0.180**	0.034	-0.005	0.035	0.082	-
	10	22.999	23.123	**22.664**	23.123	23.362	-	**0.157**	0.017	-0.005	0.023	0.087	-
pr($\times 10^{-5}$)	1	**1.648**	1.682	1.675	1.678	1.702	2.080	0.181	0.163	0.146	0.161	**0.185**	0.138
	2	**1.667**	1.735	1.725	1.733	1.742	2.097	**0.139**	0.126	0.106	0.121	0.133	0.104
	3	**1.684**	1.772	1.759	1.770	1.765	2.119	**0.117**	0.107	0.080	0.103	**0.117**	0.097
	4	**1.705**	1.803	1.784	1.796	1.786	2.151	**0.103**	0.087	0.059	0.081	0.095	0.085
	5	**1.726**	1.833	1.803	1.817	1.804	2.178	**0.093**	0.067	0.046	0.063	0.086	0.071
	6	**1.746**	1.855	1.816	1.834	1.814	-	**0.091**	0.054	0.036	0.052	0.077	-
	7	**1.777**	1.877	1.829	1.854	1.829	-	**0.080**	0.038	0.028	0.045	0.062	-
	8	**1.812**	1.893	1.842	1.872	1.840	-	**0.066**	0.018	0.017	0.028	0.047	-
	9	1.854	1.904	1.853	1.886	**1.851**	-	**0.061**	0.007	0.010	0.019	0.034	-
	10	1.908	1.912	1.863	1.899	**1.860**	-	**0.056**	-0.003	0.004	0.009	0.028	-
psl	1	**237.243**	245.675	245.801	242.856	243.295	284.758	0.351	0.309	0.249	0.301	**0.360**	0.315
	2	**243.172**	259.654	256.854	255.864	253.370	289.515	**0.274**	0.212	0.151	0.199	0.266	0.259
	3	**247.742**	267.181	261.879	262.011	256.714	290.805	0.245	0.182	0.103	0.172	**0.246**	0.244
	4	**251.438**	272.706	265.405	265.906	259.874	291.080	0.233	0.148	0.067	0.133	0.201	**0.247**
	5	**256.362**	276.614	268.287	268.545	261.215	298.682	**0.213**	0.123	0.041	0.101	0.171	0.185
	6	**259.028**	279.888	269.181	271.727	262.304	-	**0.215**	0.095	0.030	0.076	0.159	-
	7	**264.323**	282.558	271.174	274.927	264.772	-	**0.189**	0.079	0.024	0.052	0.140	-
	8	269.725	284.993	273.249	277.126	**267.130**	-	**0.185**	0.051	0.007	0.043	0.110	-
	9	276.206	286.517	274.057	278.237	**268.441**	-	**0.180**	0.029	-0.001	0.036	0.086	-
	10	284.973	288.660	273.684	279.112	**268.147**	-	**0.158**	0.008	0.000	0.027	0.088	-
v1000	1	**1.099**	1.175	1.145	1.150	1.224	-	0.217	0.197	0.166	0.194	**0.218**	-
	2	**1.112**	1.242	1.206	1.220	1.260	-	**0.167**	0.136	0.110	0.134	0.157	-
	3	**1.124**	1.285	1.241	1.260	1.274	-	0.142	0.110	0.081	0.117	**0.145**	-
	4	**1.139**	1.314	1.265	1.283	1.285	-	**0.122**	0.086	0.059	0.098	0.121	-
	5	**1.150**	1.333	1.278	1.296	1.292	-	**0.112**	0.074	0.042	0.078	0.109	-
	6	**1.161**	1.348	1.286	1.310	1.299	-	**0.112**	0.059	0.030	0.057	0.091	-
	7	**1.184**	1.360	1.293	1.322	1.309	-	**0.094**	0.052	0.030	0.046	0.071	-
	8	**1.205**	1.370	1.300	1.331	1.319	-	**0.083**	0.035	0.013	0.032	0.051	-
	9	**1.231**	1.380	1.306	1.340	1.326	-	**0.070**	0.010	0.003	0.019	0.036	-
	10	**1.258**	1.390	1.310	1.346	1.329	-	**0.063**	0.003	0.002	0.003	0.031	-
u1000	1	**1.381**	1.464	1.447	1.443	1.525	-	0.226	0.205	0.166	0.203	**0.233**	-
	2	**1.409**	1.554	1.540	1.546	1.569	-	**0.170**	0.142	0.096	0.134	**0.170**	-
	3	**1.424**	1.604	1.588	1.603	1.585	-	0.151	0.120	0.066	0.110	**0.152**	-
	4	**1.444**	1.640	1.616	1.638	1.601	-	**0.139**	0.096	0.050	0.089	0.120	-
	5	**1.460**	1.665	1.638	1.661	1.611	-	**0.132**	0.080	0.035	0.070	0.107	-
	6	**1.478**	1.684	1.649	1.678	1.617	-	**0.130**	0.064	0.022	0.056	0.099	-
	7	**1.506**	1.700	1.663	1.700	1.628	-	**0.114**	0.054	0.015	0.039	0.090	-
	8	**1.538**	1.715	1.676	1.715	1.642	-	**0.099**	0.033	0.004	0.031	0.068	-
	9	**1.572**	1.726	1.685	1.731	1.654	-	**0.094**	0.011	-0.004	0.012	0.045	-
	10	**1.615**	1.738	1.688	1.739	1.656	-	**0.083**	-0.004	-0.008	0.001	0.038	-

Region Forecasting. In Fig. 9, we give the comparison of ACC for ClimateAR and baselines in the low latitude regional forecast (i.e. 30°S to 30°N).)across 1- to 14-month lead times. The full results demonstrate that ClimateAR can significantly extend its effective forecast step over yearly in regions with greater predictability (i.e. low latitued region).

A.4.2 Visualization

To further demonstrate ClimateAR's forecasting capability across different regions, we visualize the RMSE distribution of Sea Surface Temperature (sst) and the ACC distribution of other variables in Fig. 10, 11, 13, 12. From the extensive results, we observe that ClimateAR performs particularly well in regions with high predictability (e.g., the tropics and the eastern Pacific—on seasonal scales). This highlights the model's ability to capture climate modes critical for long-term climate prediction.

A.4.3 Power Spectral Density Analyze

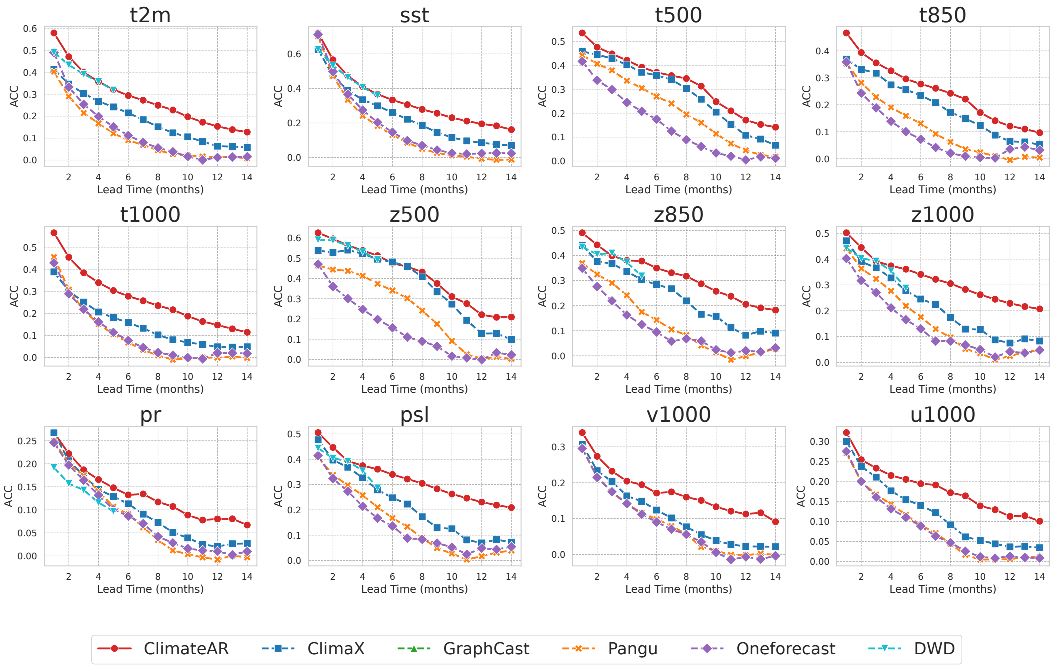

Figure 9: Comparison of ACC for ClimateAR and baselines in the low latitude regional forecast across 1- to 14-month lead times.

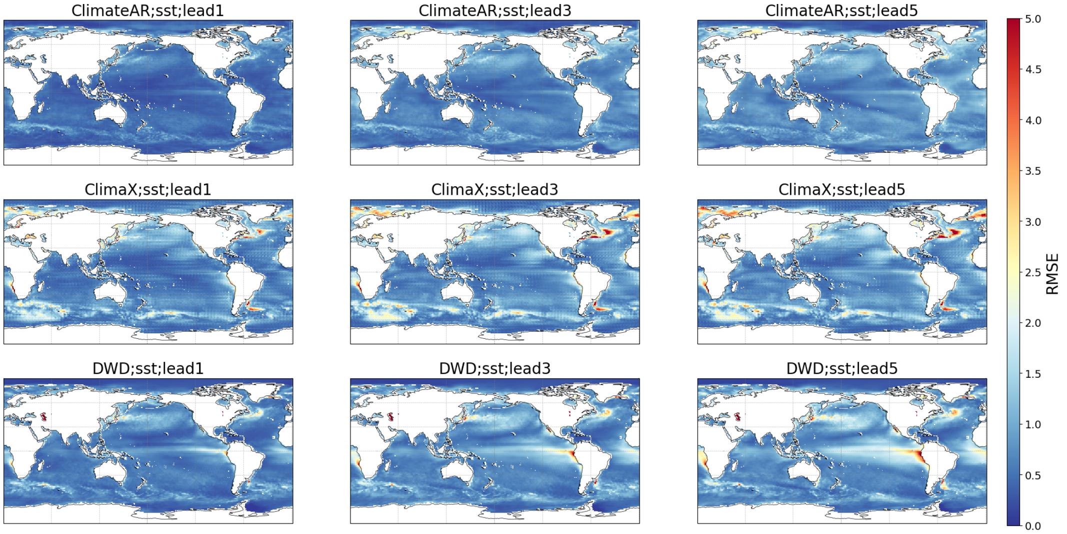

Figure 10: The global RMSE distribution of sea surface temperature forecasting with 1-, 3-, and 5-month lead times in the testing set.

We consider the power spectral density (Hickman et al., 2025) of the Niño3.4 index and Indian Ocean Dipole (IOD) index in Fig. 14. We can find that ClimateAR successfully captures the primary peaks of different climate indices at interannual timescale.

A.4.4 MULTI-SCALE PROCESSES INTERACTIONS

Global and Regional Scale. To evaluate the ability of ClimateAR to capture interactions across multiple scales, we examine the relationship between ENSO and global mean surface temperature

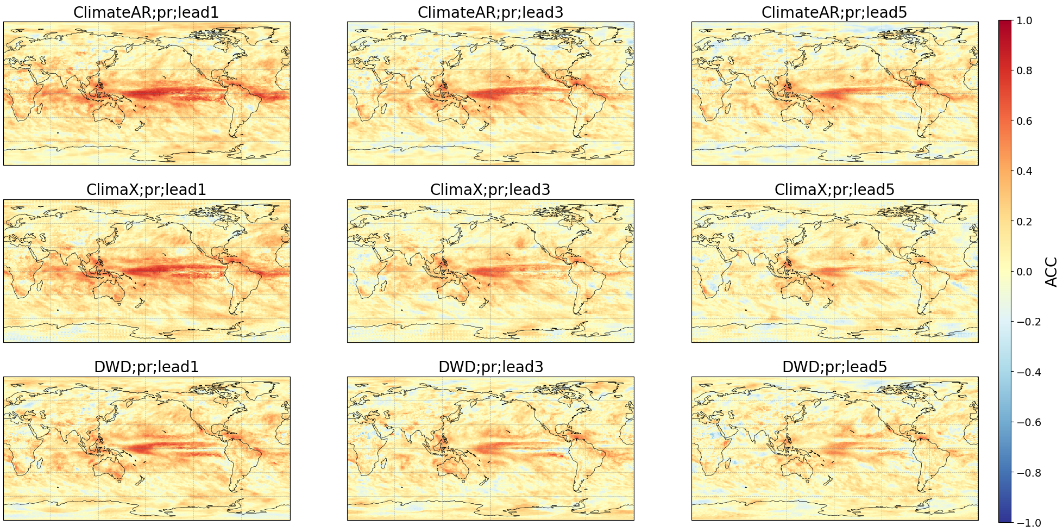

Figure 11: The global ACC distribution of precipitation rate forecasting with 1-, 3-, and 5-month lead times in the testing set.

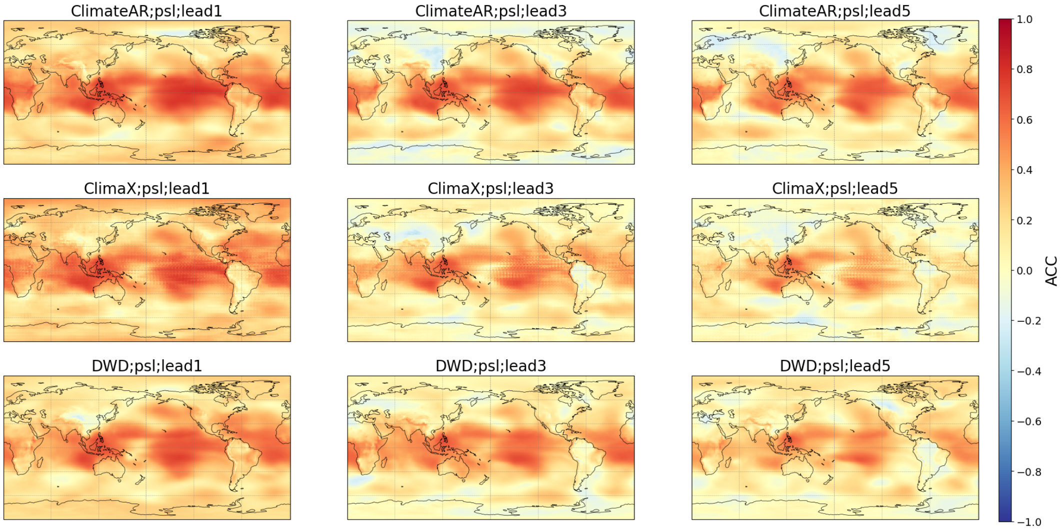

Figure 12: The global ACC distribution of sea level pressure forecasting with 1-, 3-, and 5-month lead times in the testing set.

(GMST) anomaly. In Fig. 15, we present the time series of the Niño3.4 index and GMST anomaly from both observations and predictions, together with their corresponding regression coefficients. The regression coefficients between ENSO and GMST in the predictions is nearly identical to those in the ERA5 dataset (difference less than $0.05K$), and the predicted values accurately reproduce the amplitude and phase of the observed variations. This shows that the model effectively captures the short-term temperature fluctuations associated with ENSO events and successfully reproduces the expected lagged response of GMST to ENSO forcing (typically about 3-6 months).

Regional and Local Scale. Fig. 16 shows the spatial distribution of regression coefficients between ENSO and pr/t2m anomaly at each grid. The predicted patterns closely resemble those observed. The model accurately identifies the characteristic teleconnections associated with ENSO and captures the positive or negative grid-point-level responses to ENSO intensity across the global domain.

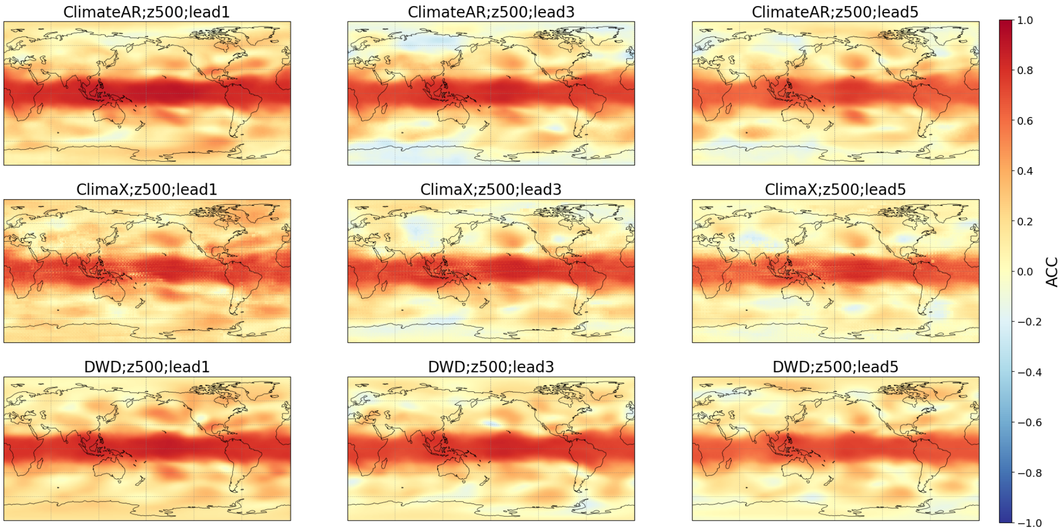

Figure 13: The global ACC distribution of 500hPa geopotential forecasting with 1-, 3-, and 5-month lead times in the testing set.

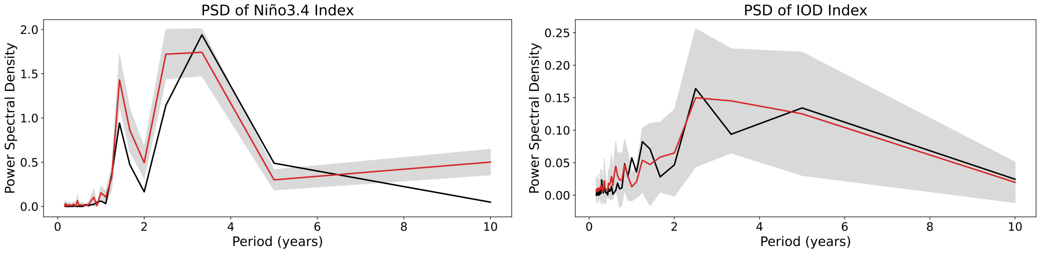

Figure 14: The Power Spectral Density (PSD) of the Niño3.4 index generated by ClaimteAR at 6-month lead time and IOD index generated by ClaimteAR at 1-month lead time and compare it with the reference data. The shaded area represents the range indicating twice the ensemble standard deviation.

Overall, GMST represents large-scale global variability, ENSO indices represents mid-scale variability, and grid-wise precipitation/t2m anomalies represents small-scale regional fluctuations. The high consistency between predicted and observed relationships across all these scales indicates that ClimateAR effectively models the interactions among climate processes and successfully captures cross-scale variability.

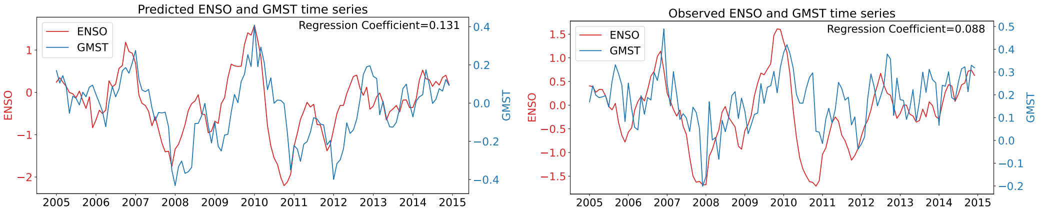

Figure 15: Comparison of the prediction ahead 1 month and observation for the global mean surface temperature (GMST) and ENSO time series.

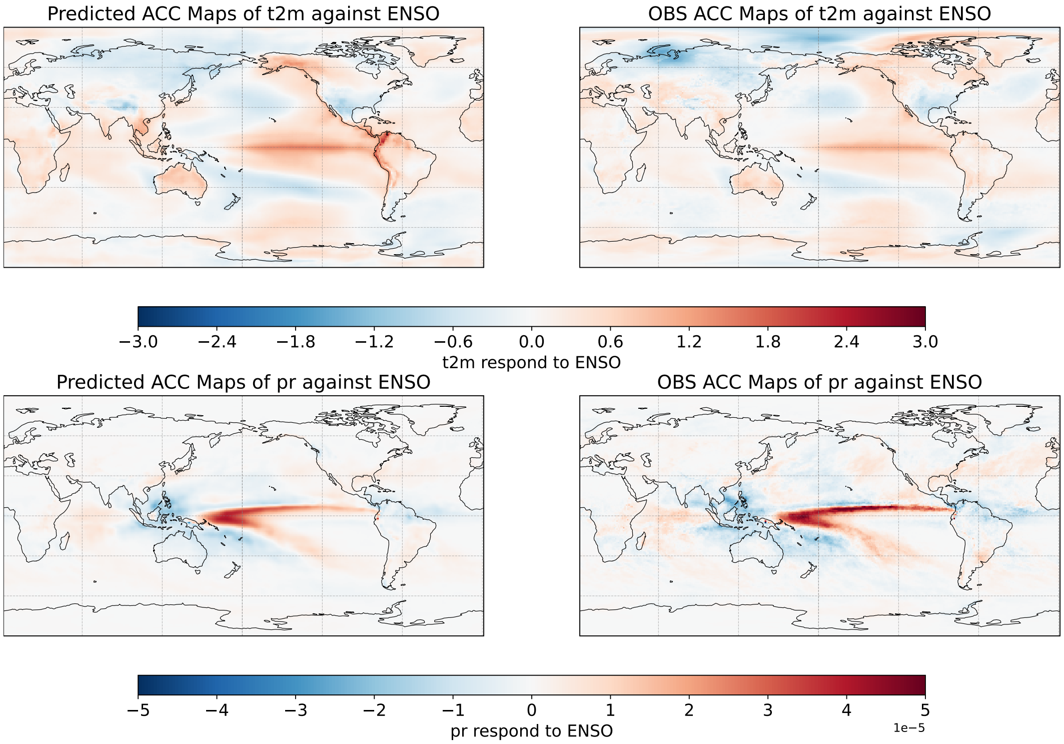
Predicted ACC Maps of t2m against ENSO
OBS ACC Maps of t2m against ENSO
−3.0
−2.4
−1.8
−1.2
−0.6
0.0
0.6
1.2
1.8
2.4
3.0
t2m respond to ENSO
Predicted ACC Maps of pr against ENSO
OBS ACC Maps of pr against ENSO
−5
−4
−3
−2
−1
0
1
2
3
4
5
1e−5
pr respond to ENSO

Figure 16: Maps of regression coefficients of predicted ahead 1 month and observed pr and t2m respond to the Niño3.4 index over 2005–2014.

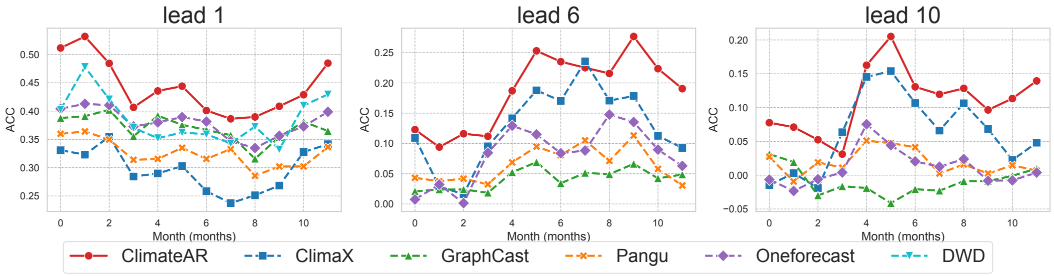

Figure 17: T2m ACC forecast starting from each month at 1-,6-,and 10-lead times.

A.4.5 Forecasting from Different Months

In Fig. 17, we use each of the 12 months in a year as a forecasting start point with lead times of 1, 6, and 10 months, respectively, and compute the average t2m forecast ACC values. It can be seen that ClimateAR achieved the best ACC level in most months. For some months that are difficult to predict (e.g., the months when the ENSO starting phase is reset), we can also get high ACC performance.

A.4.6 Hyperparameter Study

We conducted a search for two critical hyperparameters during the model's pre-training phase, including noise ratio p and number of partitions N. Specifically, p controls the noise ratio of the teach-forcing input during the training procedure, N controls the number of partitions codebooks and V controls the size of codebooks. To ensure fairness, other hyperparameters are fixed when a specific one is tuned. The details of different ACCs for different values of p and N are summarized in Table 7.

Table 7: 1 month-ahead prediction ACC for different hyperparameters of ClimateAR.

	ACC (↑)											
	noise				codebooks				codebook size			
	0.2	0.3	0.4	0.5	2	4	8	16	1024	2048	4096	8192
z500	0.408	**0.428**	0.414	0.405	0.395	0.394	**0.428**	0.398	0.402	0.408	**0.428**	0.397
t2m	0.456	**0.480**	0.462	0.466	0.445	0.455	**0.480**	0.467	0.463	0.467	**0.480**	0.466
pr	0.162	**0.190**	0.171	0.164	0.159	0.162	**0.190**	0.164	0.164	0.162	**0.190**	0.161
psl	0.348	**0.374**	0.356	0.344	0.327	0.331	**0.374**	0.335	0.350	0.350	**0.374**	0.330

Table 8: Result of efficiency study of ClimateAR and data-driven baselines.

Method	Parameters	GPU Memory (GB)	FLOPs	Training Time Min / Epoch	Inference Time s / Step	ACC
ClimaX	104.0 M	19.27	420.97 G	18.78	0.162	0.376
Oneforecast	24.7 M	38.95	548.78 G	69.73	0.516	0.386
GraphCast	28.9 M	34.59	1852.26 G	32.33	0.279	0.376
Pangu	23.9M	7.60	213.82G	5.48	0.047	0.329
ClimateAR	480.6 M	18.34	324.23 G	13.13	0.179	0.464

A.4.7 Efficiency Study

Training Cost. The training time complexities of ClimateAR are $O(h^2w^2)$, where (h, w) is the size of feature map $\mathbf{f}$. which is consistent with traditional ViTs. To conduct a fair comparison, we uniformly set the batch size to 8 when measuring the GPU memory usage.

Inference Cost. Unlike traditional autoregressive models, the inference time complexities of ClimateAR are consistent with the complexity of the training $O(h^2w^2)$, which has been demonstrated in previous paper (Tian et al., 2024). When the number of predicted members in the set is M, the complexities increases to $O(Mh^2w^2)$.

From Table 8 we can find that (1) As a generative model, ClimateAR has a lower cost than most deterministic models, which demonstrates a competitive efficiency. (2) Due to the patch-based processing, the training time of ClimaX, Pangu, and ClimateAR is significantly lower than that of deterministic graph-based models.

A.5 Rolling Fine-tune

On ERA5 dataset, we use the model to generate predictions for 1 to 3 steps in a rolling fashion and then mix these predictions into our sample input. This allows the model to get the ability to correct accumulated errors as it optimizes the loss function with a biased input. After rolling fine-tuning procedure, we successfully mitigated the RMSE drift of the model, and some of the results are summarized in Fig. 18.

A.6 Additional Relate Work

AutoRegressive Models. AutoRegressive models have achieved significant success in language and visual generation tasks (Radford et al., 2019; Bai et al., 2024). Early visual AR models generate images at pixel level row-by-row (Van den Oord et al., 2016; Van Den Oord et al., 2016; Chen et al., 2020), whereas later models inspired by ViT (Dosovitskiy et al., 2021) generate images at patch level row-by-row (Esser et al., 2021; Lee et al., 2022). Recent advances in visual AR models based on next-scale prediction (Tian et al., 2024) have significantly improved generative quality and speed, and demonstrated scaling capabilities comparable to large language models (LLMs) (Kaplan et al., 2020; Hoffmann et al., 2022). Compared to diffusion models, AR models exhibit superior efficiency in both training and inference, and are particularly advantageous for fusing complex multimodal conditional information with discrete tokens (Yu et al., 2023; Lu et al., 2023). While diffusion-based generative models (Price et al., 2025; Oskarsson et al., 2024) and deterministic models(Nguyen et al., 2023; Bi et al., 2023) have been extensively explored for weather and climate forecasting, the potential of AR generative models in long-term climate forecasting remains underexplored.

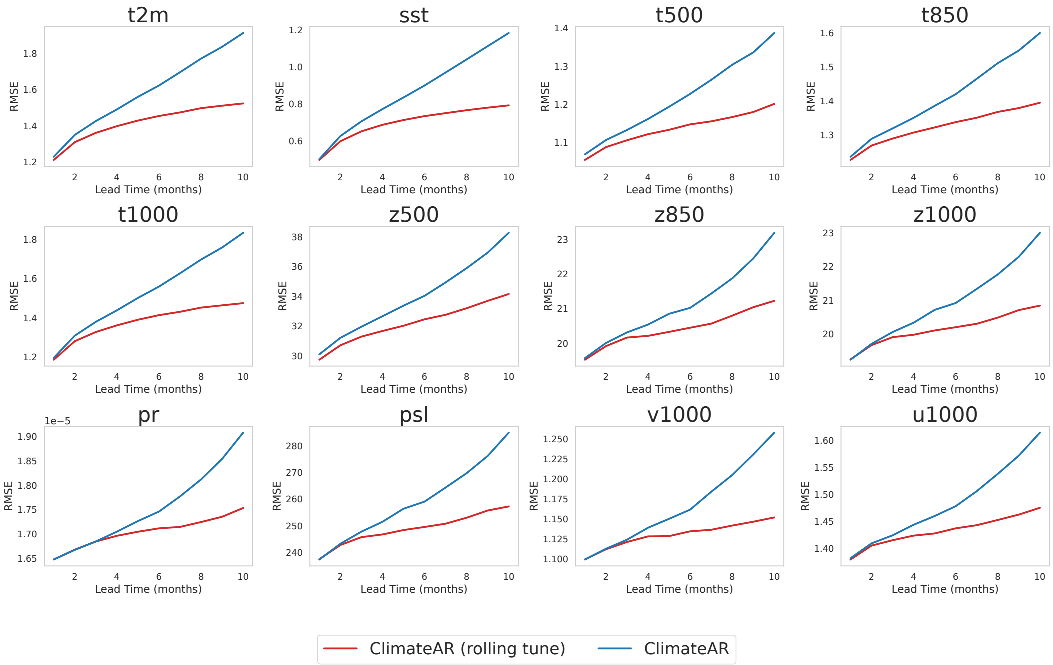

Figure 18: Comparison of global forecast RMSE for ClimateAR before and after rolling fine-tuning across 1- to 10-month lead times.

A.7 Limitation and Future Work

Despite such advantages, there are several directions that remain to be explored in the future: (1) fine-tuning the model to reduce the cumulative loss in iterative forecasts; (2) incorporating contrastive learning or classifier-free guidance techniques in generative models to enhance the model's ability to predict anomalies; and (3) using ClimateAR to assist in more tasks than forecasting such as dimensionality reduction analysis and anomaly detection.